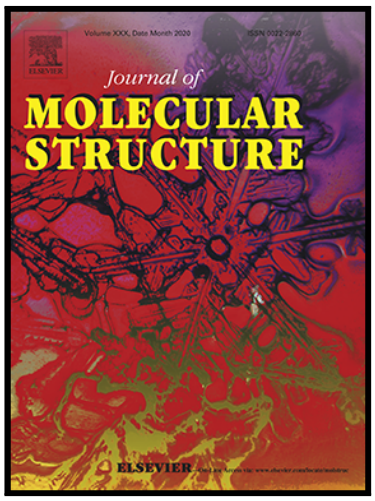

Novel derivatives of aroylacrylic acid phenylamides as inducers of apoptosis through the ROS-mediated pathway in several cancer cell lines

Tamara B. Vujatović , Maja D. Vitorović-Todorović , Ilija Cvijetić , Tamara Vasović Writing - review & editing , Milan R. Nikolić Investigation , Irena Novaković , Snežana Bjelogrlić

PII: S0022-2860(21)01828-7
DOI: https://doi.org/10.1016/j.molstruc.2021.131702
Reference: MOLSTR 131702

To appear in: *Journal of Molecular Structure*

Received date: 26 July 2021
Revised date: 2 October 2021
Accepted date: 10 October 2021

Please cite this article as: Tamara B. Vujatović , Maja D. Vitorović-Todorović , Ilija Cvijetić , Tamara Vasović Writing - review & editing , Milan R. Nikolić Investigation , Irena Novaković , Snežana Bjelogrlić , Novel derivatives of aroylacrylic acid phenylamides as inducers of apoptosis through the ROS-mediated pathway in several cancer cell lines, *Journal of Molecular Structure* (2021), doi: https://doi.org/10.1016/j.molstruc.2021.131702

Novel derivatives of aroylacrylic acid phenylamides as inducers of apoptosis through the ROS-mediated pathway in several cancer cell lines

Tamara B. Vujatović,[a,c] Maja D. Vitorović-Todorović,[a*] Ilija Cvijetić,[b] Tamara Vasović,[c] Milan R. Nikolić,[c] Irena Novaković,[d] Snežana Bjelogrlić[e]

[a]*Military Technical Institute, Ratka Resanovića 1, Belgrade, Serbia*

[b]*University of Belgrade - Faculty of Chemistry, Studentski trg 12-16, Belgrade, Serbia*

[c]*Department of Biochemistry, University of Belgrade - Faculty of Chemistry, Studentski trg 12-16, Belgrade, Serbia*

[d]*University of Belgrade - Institute of Chemistry, Technology and Metallurgy - National Institute of the Republic of Serbia, ICTM, Njegoševa 12, Belgrade, Serbia*

[e]*National Cancer Research Center, Pasterova 14, Belgrade, Serbia*

Corresponding author: Maja D. Vitorović-Todorović, PhD

mvitod@chem.bg.ac.rs, majavitod@gmail.com, Phone: +381 11 3401 255

Graphical abstract:

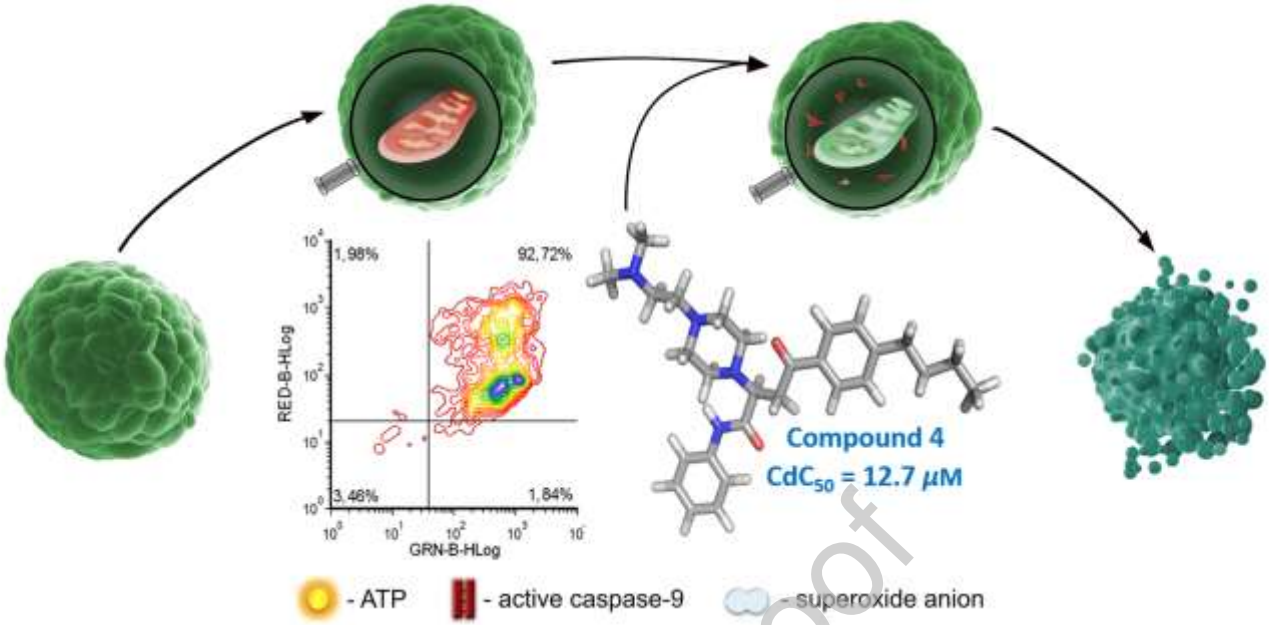

Highlights:

- Novel Michael's adducts of aroylacrylic acid phenylamides have been synthesized.
- The majority of compounds activated intrinsic apoptotic pathways.
- Compounds showed moderate *in vivo* toxicity toward *Artemia salina.*
- Compound **4** had superior antibacterial activity comparing to chloramphenicol.

Abstract

In the present work, the α,β-double bond of the aroylacrylic acid phenylamides was suitably modified to optimize the toxicity–antiproliferative activity ratio of the resulting compounds **1-5**. The phenylamides were modified by Michael's addition of suitably chosen piperidine-containing fragments: 1-amino-*N*-benzylpiperidine (**a1**), 4-benzylpiperidine (**a2**), and *N*,*N*-dimethyl-*N*-[2-(1-piperazinyl)-ethyl]amine (**a3**). The compounds exerted micromolar activity toward three cancer cell lines, A549, LoVo, and Skov-3, causing apoptotic cell death. It was shown that the nature of the cyclic amine moiety at position C2 of the compounds is probably the primary determinant of anticancer activity toward tested cell lines and the acute toxicity toward brine shrimp (*Artemia salina*). The majority of compounds revealed the ability to vigorously induce mitochondrial superoxide anion generation in all treated cell lines, which together with cell cycle arrest at the S phase and activation of intrinsic caspase cascade, indicates the possibility that apoptosis was triggered due to irreparable chromosomal damage by acute oxidative stress. Two derivatives also exerted significant antibacterial activity with one order of magnitude more potent than chloramphenicol in most of the investigated bacterial strains. Also, the drug-like properties for all compounds were estimated by available software tools.

Keywords: aroylacrylic acid phenylamides, Michael's addition, piperidine, anticancer activity, apoptosis, antibacterial activity.

1. Introduction

The small α,β-unsaturated carbonyl compounds such as chalcones, their derivatives 4-aminochalcone maleamic acids and imides, phenylcinnamides, aroylacrylic acids, and their phenylamides exert a wide variety of biological activities, in particular antioxidative, antimalarial, antileishmanial, anti-inflammatory and anticancer activities (**Scheme 1**). The health benefits of natural chalcones can be ascribed to their redox properties and the ability to scavenge radical oxygen species [1]. Along with scavenging free radicals, the biological activity of chalcones, and other small α,β-unsaturated compounds can be ascribed to their ability to act as Michael's acceptors of nucleophilic moieties, particularly the thiol groups of biological targets. Chalcones and structurally similar compounds exert antiproliferative activity through various mechanisms. For example, recently described chalcone-based compounds that are proteasome inhibitors probably act as covalent binders via ketovinyl

moiety [2]. It has been confirmed that *N*-alkylmaleimides exert antiproliferative activity by inhibiting topoisomerase I [3],[4]. Some of these α,β-unsaturated carbonyl compounds may act as anti-tubulin agents [5],[6].

Previously, we have been working on aroylacrylic acids that revealed potent anticancer properties [7], which motivated us to proceed with the design and synthesis of aroylacrylic acid phenylamides as chalcone-aroylacrylic acid chimeras by incorporation of the amidic moiety between the α,β-unsaturated carbonyl moiety and the B ring of chalcones (**Scheme 1**) [8]. The majority of these derivatives showed sub-micromolar anticancer activity toward several cancer cell lines. However, these compounds also exerted significant *in vivo* acute toxicity confirming that further structural optimization was required to obtain less toxic compounds. We hypothesized that observed toxicity was a consequence of alkylating action of the phenylamides. Therefore, in the present work, we suitably modified the α,β-double bond of the aroylacrylic acid phenylamides to avoid possible alkylating action of the phenylamides of the various biological targets. The compounds were modified by Michael's addition of selected piperidine-containing fragments: 1-amino-*N*-benzylpiperidine (**a1**), 4-benzylpiperidine (**a2**) and *N*,*N*-dimethyl-*N*-[2-(1-piperazinyl)ethyl]amine (**a3**) to the α,β-double bond of the phenylamides, yielding five novel compounds, **1-5**. These piperidine fragments seemed like a suitable choice for Michael's addition since several FDA approved anticancer agents or those that are in the clinical trials contain highly functionalized piperidine moiety, for instance: Alvocidib [9] (Sanofi, CDK 1/4/9 inhibitor, phase II clinical trials), AT-7519 [10] (Astex, CDK 2/5/9 inhibitor, phase II clinical trials), Alecensa [11] (Genentech INC., Multikinase inhibitor, FDA approved) and Imbruvica [12] (Pharmacyclics/Janssen Biotech, Bruton's tyrosine kinase inhibitor, FDA approved), **Scheme 2**. Other examples of piperidine-containing compounds with proven activity toward molecular cancer targets can be found in the review article of Goel and co-authors [13].

The present study aims to investigate the anticancer and antimicrobial properties of the above-described compounds, and estimate their toxicity and drug-likeness. Results presented herein provide the first insight into the biological activity profile and a guideline for future investigations on intracellular metabolic transformation, target identification, and the exact mechanism of biological action.

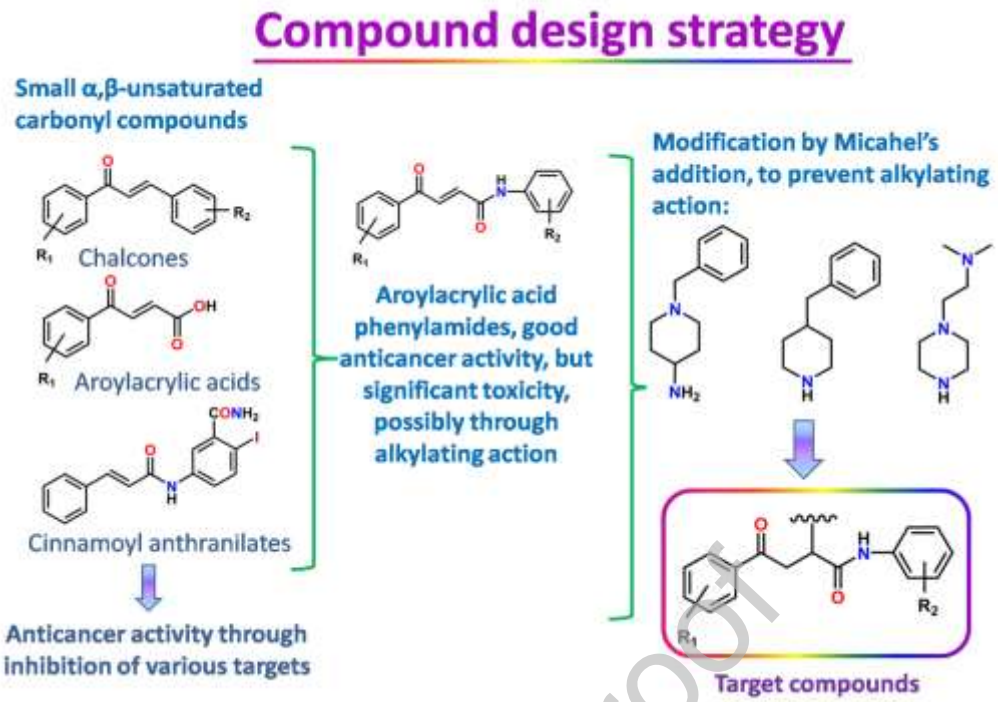

Scheme 1. The design strategy for **1**-**5**: By combining chalcones, aroylacrylic acid, and cinnamoyl anthranilates, the phenylamides of aroylacrylic acids were previously designed and synthesized [8]. Compounds exerted significant anticancer activity, but they exhibited significant toxicity, possibly due to their alkylating action. Compounds were further modified by Michael's addition of suitably chosen piperidine fragments, to prevent their toxicity. This synthetic procedure yielded novel compounds, **1**-**5**.

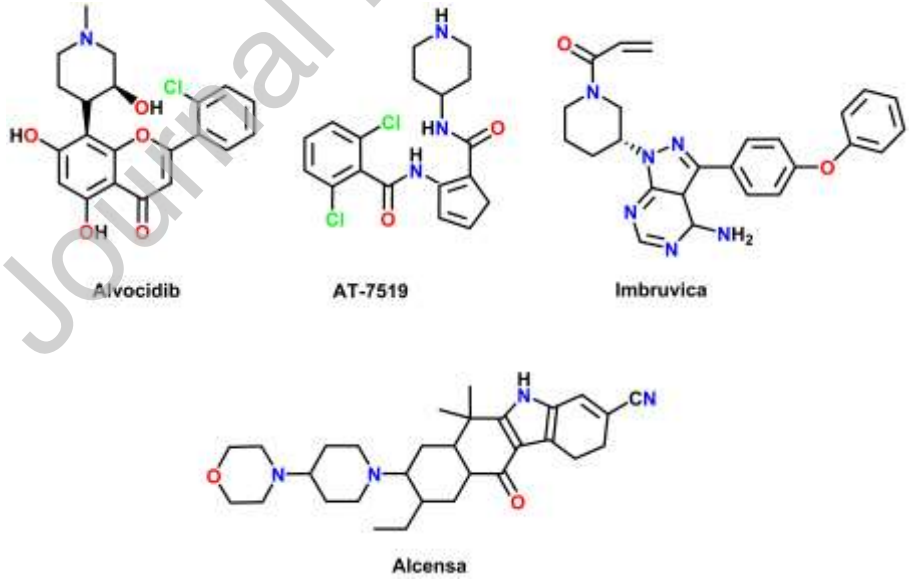

Scheme 2. Examples of anticancer agents comprising highly functionalized piperidine moiety: Alvocidib (Sanofi, CDK 1/4/9 inhibitor; phase II clinical trials), AT-7519 (Astex, CDK 2/5/9 inhibitor; phase II clinical trials), Alcensa (Genentech INC., Multikinase inhibitor; FDA approved) and Imbruvica (Pharmacyclics/Janssen Biotech, Bruton's tyrosine kinase inhibitor; FDA approved).

2. Materials and methods

2.1. Chemistry

All chemicals were purchased from Sigma Aldrich or Merck and were used as received. The ^{1}H and ^{13}C NMR spectra were recorded in $CDCl_3$ or d_6-DMSO on Bruker AVANCE400/101 MHz instrument. Chemical shifts are reported in parts per million (*ppm*) relative to tetramethylsilane (TMS) as an internal standard. Spin multiplicities are given as follows: *s* (singlet), *d* (doublet), *t* (triplet), *m* (multiplet). High-resolution mass spectra were recorded on the LTQ Orbitrap XL instrument, in positive mode, with direct injection of the sample. Synthetic procedures for aroylacrylic acid amides were already described in the literature [8].

2.1.1. Synthesis procedures and characterization of the compounds

Synthesis procedure for **2-(1-Benzyl-4-piperidinylamino)-4-(4-chlorophenyl)-4-oxo-*N*-phenylbutanoylamide (1):** (2*E*)-4-(4-chlorophenyl)-4-oxo-2-*N*-phenylbutenamide (0.2 g, 0.7 mmol) was dissolved in methylene chloride (5 mL) at room temperature, then the equimolar amount of 1-benzyl-4-piperidinamine (150 μL) and 5 mL of toluene were added. The mixture was stirred at room temperature for 24^{h}. Solvents were removed under reduced pressure. The obtained crude product was washed with *n*-hexane to give the final compound as a white solid with a reaction yield of 55% and Mp=116-118 °C. ^{1}H NMR (400 MHz, $CDCl_3$): δ 9.58 (*s*, 1H, amido-NH), 7.83 (*d*, *J* = 8.6 Hz, 2H, aroyl-*o*-phenyl), 7.49 (*d*, *J* = 7.7 Hz, 2H, amido-*o*-phenyl), 7.36 (d, *J* = 8.6 Hz, 2H, aroyl-*m*-phenyl), 7.24 (overlapped *m*, 6H, amido-*m*-phenyl and benzyl-*o*- and *m*-phenyl), 7.19 (*m*, 1H, benzyl-*p*-phenyl), 7.03 (*t*, *J* = 7.4 Hz, 1H, amido-*p*-phenyl), 3.67 (*dd*, *J* = 8.1, 3.3 Hz, 1H, ABX), 3.48 (*dd*, *J* = 17.2, 3.3 Hz, 1H, ABX), 3.43 (*s*, 2H, benzyl-CH_2-), 3.21 (*dd*, *J* = 17.2, 8.1 Hz, 1H, ABX), 2.83 – 2.73 (*m*, 2H, piperidinyl-CH_2-), 2.51(*m*, 1H, piperidinyl-CH-), 2.09 (*s*, 1H, amino-NH-) 1.97 (*t*, *J* = 10.8 Hz, 2H, piperidinyl-CH_2-), 1.78 (*m*, 2H, piperidinyl-CH_2-), 1.50 – 1.39 (*m*, 2H, piperidinyl-CH_2-). ^{13}C NMR (101 MHz, $CDCl_3$) δ 197.26, 172.06, 140.19, 137.60, 134.63, 129.66, 129.19, 129.10, 129.03, 128.31, 128.25, 127.14, 124.22, 119.32, 62.93, 57.10, 54.35, 52.02, 41.01, 32.93, 32.69, 30.89. HR MS (ESI): Obs. 476.21159 (M + 1), Calc. 476.21048

Synthesis procedure for **4-(4-Chlorophenyl)-2-[4-(2-dimethylaminoethyl)-1-piperazinyl]-4-oxo-*N*-phenylbutanoylamide (2):** (2*E*)-4-(4-chlorophenyl)-4-oxo-*N*-phenyl-2-butenamide (0.2 g, 0.7 mmol) was dissolved in methylene chloride (5 mL) at room temperature, then *N*,*N*-dimethyl-*N*-[2-(1-piperazinyl)ethyl]amine (135 μL, 0.85 mmol) and 5

mL of toluene were added. The mixture was stirred at room temperature for 24^{h}, then filtered off and solvents were removed under reduced pressure, and obtained semi-solid substance was purified by silica gel dry-flash column chromatography ($CHCl_3$: MeOH : NH_4OH = 7 : 3 : 0.07). The pure compound was obtained as orange semi-solid with a reaction yield of 47%. ^{1}H NMR (400 MHz, $CDCl_3$) δ 9.14 (*s*, 1H, amido-NH), 7.88 (*d*, *J*= 8.6 Hz, 2H, aroyl-*o*-phenyl), 7.46 – 7.35 (overlapped *m*, 4H, aroyl-*m*-phenyl and amido-*o*-phenyl), 7.26 – 7.18 (*m*, 2H, amido-*m*-phenyl), 7.02 (*t*, *J* = 7.4 Hz, 1H, amido-*p*-phenyl), 4.24 (*dd*, J = 7.9, 4.2 Hz, 1H, ABX), 3.61 (*dd*, J = 16.5, 7.9 Hz, 1H, ABX), 2.84 (*dd*, *J* = 16.5, 4.2 Hz, 1H, ABX), 2.62 (*br*, 4H, ethylamino-CH_2), 2.53 (*br*, 8H, piperazinyl-CH_2-), 2.32 (*br*, 6H, methylamino-CH_3). ^{13}C NMR (101 MHz, $CDCl_3$) δ 197.19, 169.78, 139.52, 137.59, 135.45, 129.71, 129.25, 129.03, 128.91, 128.22, 124.22, 119.37, 65.10, 56.27, 55.64, 54.04, 45.36, 31.87. HR MS (ESI): Obs. 443.22184 (M + 1), Calc. 443.22138

Synthesis procedure for **2-[4-(2-Dimethylaminoethyl)-1-piperazinyl]-4-(3,4-dimethyl-phenyl)-*N*-(4-isopropylphenyl)-4-oxo-butanoylamide (3):** (2*E*)-4-(3,4-dimethylphenyl)-4-oxo-*N*-[4-(2-propyl)phenyl]-2-butenamide (0.2 g, 0.62 mmol) was dissolved in methylene chloride (5 mL) at room temperature, then *N*,*N*-dimethyl-*N*-[2-(1-piperazinyl)ethyl]amine (120 μL, 0.75 mmol) and 5 mL of toluene were added. The mixture was stirred at room temperature for 24^{h}. Solvents were removed under reduced pressure and the obtained semi-solid substance was characterized without purification. The compound was obtained as orange semi-solid in quantitative yield. ^{1}H NMR (400 MHz, $CDCl_3$) δ 9.23 (*s*, 1H, amido-NH), 7.80 (*s*, 1H, aroyl-*o*-phenyl), 7.76 (*d*, *J* = 8.0 Hz, 1H, aroyl-*o*-phenyl), 7.47 (*d*, *J* = 8.4 Hz, 2H, amido-*o*-phenyl), 7.23 (*d*, *J* = 7.8 Hz, 2H, amido-*m*-phenyl), 7.18 (*d*, *J* = 8.3 Hz, 1H, aroyl-*m*-phenyl), 4.33 (*dd*, *J* = 6.9, 5.0 Hz, 1H, ABX), 3.71 (*dd*, *J* = 16.8, 6.9 Hz, 1H, ABX), 3.03 (*dd*, *J* = 16.8, 5.0 Hz, 1H, ABX), 2.94 – 2.83 (*m*, *J* = 13.8, 6.9 Hz, 1H, *i*-Pr-CH-), 2.69 (s, 4H, ethylamino-CH_2-), 2.56 (*dd*, *J* = 19.7, 6.2 Hz, 8H, piperazinyl-CH_2-), 2.34 (overlapped *m*, 12H, aroyl-CH_3 and aminomethyl-CH_3), 1.24 (*d*, 6H, *i*-Pr-CH_3). ^{13}C NMR (101 MHz, $CDCl_3$) δ 206.83, 198.09, 169.89, 144.78, 142.56, 136.86, 135.50, 134.93, 129.82, 129.41, 129.02, 128.21, 126.83, 125.96, 119.44, 64.66, 56.55, 56.09, 54.17, 45.57, 33.59, 32.14, 30.88, 24.02, 19.98, 19.76. HR MS (ESI): Obs. 479.33967 (M + 1), Calc. 479.33860

Synthetic procedure for **2-[4-(2-dimethylaminoethyl)-1-piperazinyl]-4-(4-butyl-phenyl)-4-oxo-*N*-phenylbutanoylamide (4):** (2*E*)-4-(4-butylphenyl)-4-oxo-*N*-phenyl-2-butenamide (0.2 g, 0.62 mmol) was dissolved in methylene chloride (5 mL) at room temperature, then *N*,*N*-dimethyl-*N*-[2-(1-piperazinyl)ethyl]amine (120 μL, 0.75 mmol) and 5

mL of toluene were added. The mixture was stirred at room temperature for 24^{h}. Solvents were removed under reduced pressure, and the obtained semi-solid substance was purified by silica gel dry-flash column chromatography ($CHCl_3$: MeOH : NH_4OH = 7 : 3 : 0.07). Pure compound was obtained as pale yellow semi-solid with a reaction yield of 78%. ^{1}H NMR (400 MHz, $CDCl_3$) δ 9.21 (*s*, 1H, amido-NH), 7.85 (*d*, J = 8.2 Hz, 2H, aroyl-*o*-phenyl), 7.46 (*d*, J = 7.7 Hz, 2H, amido-*o*-phenyl), 7.27 – 7.15 (overlapped *m*, 4H, amido-*m*- and aroyl-*m*-phenyl), 7.01 (*t*, J = 7.4 Hz, 1H, amido-*p*-phenyl), 4.25 (*dd*, *J* = 7.1, 4.8 Hz, 1H, ABX), 3.63 (*dd*, *J* = 16.8, 7.1 Hz, 1H, ABX), 2.93 (*dd*, *J* = 16.8, 4.8 Hz, 1H, ABX), 2.68 – 2.40 (*m*, 14H, aminoethyl-CH_2-, piperazinyl-CH_2- and *n*-butyl-CH_2-), 2.28 (*s*, 6H, aminomethyl-CH_3), 1.60 – 1.47 (*m*, 2H, *n*-butyl-CH_2), 1.35 – 1.22(*m*, *J* = 14.6, 7.3 Hz, 2H, *n*-butyl-CH_2-), 0.86 (*t*, J = 7.3 Hz, 3H, *n*-butyl-CH_3). ^{13}C NMR (101 MHz, $CDCl_3$) δ 197.89, 170.03, 148.82, 137.75, 134.71, 128.99, 128.66, 128.40, 124.08, 119.33, 64.77, 56.47, 55.95, 54.15, 45.52, 35.69, 33.22, 32.01, 22.30, 13.88. HR MS (ESI): Obs. 465.32380 (M + 1), Calc. 465.32295

Synthesis procedure for **2-(4-Benzyl-1-piperidinyl)-*N*-(3,5-dimethoxyphenyl -4-oxo-*N*-phenyl-4-(5,6,7,8-tetrahydronaphthalenyl)butyramide (5):** (2*E*)-4-oxo-*N*-phenyl-4-(5,6,7,8-tetrahydronaphthalenyl)butenamide (0.2 g, 0.65 mmol) was dissolved in methylene chloride (5 mL) at room temperature, then 4-benzylpiperidine (140 μL, 0.8 mmol) and 5 mL of toluene were added. The mixture was stirred at room temperature for 24^{h}. Solvents were removed under reduced pressure, and the obtained solid substance was characterized without purification. The compound was obtained as pale yellow semi-solid with quantitative yield. ^{1}H NMR (400 MHz, CDCl3) δ 9.44 (*s*, 1H, amido-NH), 7.75 (*d*, J = 6.1 Hz, 2H, aroyl-*o*-phenyl), 7.57 (*d*, J = 7.7 Hz, 2H, amido-*o*-phenyl), 7.38 – 7.08 (*m*, 9H, benzyl-phenyl-CH, aroyl-*m*-phenyl, amido-*m*- and amido-*p*-phenyl), 4.32 (*dd*, J = 6.9, 5.3 Hz, 1H, ABX), 3.70 (*dd*, J = 16.6, 6.9 Hz, 1H, ABX), 2.98 (*dd*, J = 16.6, 5.3 Hz, 1H, ABX), 2.82 (*d*, J = 13.5 Hz, 4H, tetralinyl-CH_2-), 2.60 (*d*, J = 7.1, 2.2 Hz, 2H, benzyl-CH_2-), 2.53 – 2.43 (*m*, 2H, piperidinyl-CH_2-), 2.30 – 2.19 (*m*, *J* = 11.3, 9.7 Hz, 2H, piperidinyl-CH_2-), 1.84 (*s*, 4H, tetralinyl-CH_2-), 1.61 – 1.52 (*m*, J = 14.4, 7.2, 3.6 Hz, 1H, piperidinyl-CH-), 1.49 – 1.38 (*m*, J = 24.1, 11.9, 3.9 Hz, 2H, piperidinyl-CH_2-), 1.34 – 1.22 (*m*, 2H, piperidinyl-CH_2-). ^{13}C NMR (101 MHz, $CDCl_3$) δ 198.52, 170.58, 143.19, 140.32, 137.46, 134.55, 129.37, 129.19, 129.07, 128.99, 125.98, 123.98, 119.34, 65.47, 52.84, 48.08, 43.11, 37.63, 33.19, 32.92, 32.07, 29.66, 29.42, 22.99, 22.87. HR MS (ESI): Obs. 481.28719 (M + 1), Calc. 481.28550

2.2. Biological studies

2.2.1. Cell cultures

Human colorectal adenocarcinoma (LoVo, ATCC® CCL-229™), human ovary adenocarcinoma (SkOV-3, ATCC® HTB-77™), human lung non-small cell carcinoma (A549, ATCC® CCL-185™), human mammary adenocarcinoma (MCF-7, ATCC® HTB-22™), human hepatocellular carcinoma (HepG2, ATCC® HB-8065™), and human pancreatic adenocarcinoma (AsPC1, ATCC® CRL-1682™) cell lines were generously gifted by Transgene SA (Illkirch, Strasbourg, France). HaCaT fibroblasts were purchased from CLS Cell Lines Service GmbH (Eppelheim, Germany; cat. no. 300493). All cell lines were maintained in DMEM high glucose medium (Dominique Dutscher; cat.no. L0102-500), supplemented with 10% (v/v) heat-inactivated fetal bovine serum (FBS, Life Technologies; cat. no. 10270-106) and 1% (v/v) penicillin-streptomycin (10 000 units/mL and 10 000 μg/mL, Life Technologies; cat. no. 15140-122). Cells were kept at 37°C in a humidified atmosphere containing 5% (v/v) CO_2 during their exponential growth phase and incubation with investigated compounds.

Investigated compounds were initially dissolved in DMSO as a stock concentration of 20 mM, and further dilutions were prepared in DMEM complete medium. The final concentration of DMSO with cells never exceeded 0.5% (v/v).

2.2.2. Calcein AM (CAM) and propidium iodide (PI) staining

Cells were seeded in 96 flat bottom well plates (Corning® Costar®; cat. no. CLS3596) in 0.1 mL volume and left overnight to settle. On the next day, 0.05 mL of investigated compounds were added to final concentrations of 30, 50, 75, and 100 μM per well. Cells treated with 0.5% DMSO were used as a negative control. Cells were incubated with investigated compounds for 24 h, when Calcein-AM (CAM, Merck; cat.no. 206700) and propidium iodide (PI, Sigma-Aldrich; cat. no. P4170) were added in final concentrations of 0.5×10^{-3} g/mL and 1×10^{-6} g/mL respectively, and left for 30 min at room temperature in the dark. Results were monitored on a Celigo® imaging cytometer (Nexcelom Bioscience LLC, Lawrence, MA, USA) using green and red fluorescent channels.

2.2.3. Annexin V and PI staining

Cells were seeded in 96 flat bottom well plates (Corning® Costar®; cat. no. CLS3596) in 0.1 mL volume (100 000 cells/mL) and left overnight to settle. The next day, 0.05 mL of investigated compounds were added up to final concentrations from 1-75 μM per well. Cells treated with 0.5% DMSO and cells treated with Celastrol (Enzo Life Sciences; cat. no. ALX-350-332-M025) at 50 μM were used as negative and positive controls, respectively.

After 24^{h} of incubation, a supernatant medium with non-adherent cells was removed from each well and placed into another 96 well plates. Ethylenediaminetetraacetic acid (EDTA, Sigma-Aldrich, Cat. No. 03609) 2 mM in saline (w/v) was added to wells with remaining adherent cells, and the plate was incubated for 15 min at 37ºC. Afterward, the plate was centrifuged (450 x g for 10 min), the supernatant discarded, and 200 μL of trypsin-EDTA (BioWest; cat. no. L0930-100) added to each well. Cells were detached in about 15 min of incubation at 37ºC. Trypsin-EDTA was discarded after an additional spinning cycle when previously removed supernatants with non-adherent cells were turned back to trypsinized cells. Such prepared samples were stained with Annexin V-FITC (Immuno Tools; cat. no. 31490013) and PI (MiltenyiBiotec; cat. no. 130-093-233) each in a volume of 3 μL. The trypsinization here described protocol was applied every time cells were prepared for flow cytometry analyses unless it is stated otherwise.

Plates were analyzed on Guava® easyCyte 12HT Benchtop flow microcapillary cytometer (Luminex, Austin, Texas, USA) using the dedicated InCyte® software package. Cells were categorized according to Annexin V-FITC (green fluorescence) and PI (red fluorescence) labeling on viable (double negative), cells in the early phase of apoptotic death (Annexin V-FITC single-stained cells), necrotic cells (PI single-stained cells), and cells in advanced phases of cell death (double-stained cells).

Results from Annexin V/PI readouts were further used to generate concentration-response curves for cell death response. Percentages of all cells stained with either Annexin V and/or PI were summarized for each treated sample and plotted against corresponding concentration, and curves were computed using a sigmoidal asymmetric five-parameter logistic equation in GraphPad Prism 6 software (GraphPad Software, San Diego, CA, USA). Cell death concentration (CdC_{50}) is the one that induces death in 50% of treated cells.

2.2.4. Evaluation of sub-G1 area

After Annexin V/PI reading was over, plates with remaining cells were centrifuged (450 x g for 10 min), the supernatant discarded, and 200 μL of 70% ethanol was added to cells. The plates were left overnight at 4ºC. On the next day, the plates were centrifuged at 450 x g for 10 min, ethanol was discarded, and RNAse-A in PBS was added to wells (0.5 x 10^{-6} g/mL, final concentration). After the plates were incubated at 37ºC for 1^{h}, cells were stained with PI (1×10^{-6} g/mL final concentration) and kept in the dark at room temperature for 30 min before analysis. Cells were acquired on Guava® easyCyte 12HT Benchtop flow

microcapillary cytometer, and the population was analyzed with the dedicated InCyte® software package.

2.2.5. Cell cycle analysis

Cells were seeded in 96 flat bottom well plates (Corning® Costar®; cat. no. CLS3596) in 0.1 mL volume (100 000 cells/mL) and left overnight to settle. On the next day, 0.05 mL of investigated compounds were added up to final concentrations from 1-75 μM per well and incubated for 12^{h}. Cells treated with 0.5% DMSO were used as negative controls. At the end of incubation, 96-well plates with investigated samples were centrifuged (450 x g for 10 min), and the media was discarded. Cells were detached by trypsin treatment and fixed with 70% ethanol overnight, followed by RNAse-A treatment and PI staining as described above. Cells were acquired on Guava® easyCyte 12HT Benchtop flow microcapillary cytometer, and populations were analyzed with the dedicated InCyte® software package.

2.2.6. Determination of cellular activated caspase-8 or/and caspase-9

Cells were seeded in 96 flat bottom well plates in 0.1 mL volume (100 000 cells/mL) and left overnight to settle. On the next day, 0.05 mL of investigated compounds were added up to final concentrations of 50 μM per well and incubated for 6^{h}. Cells treated with 0.5% DMSO were used as negative controls. Cells were detached by trypsin treatment and analyzed for activated caspase-8 (CaspGLOW™ fluorescein active caspase-8 staining kit, BioVision; cat. no. K188-25) and caspase-9 (CaspGLOW™ red active caspase-9 staining kit, BioVision; cat. no. K199-25) following manufacturer's instructions on Guava® easyCyte 12HT Benchtop flow microcapillary cytometer. The statistical evaluation has been performed using an unpaired *t*-test with Welch's correction comparing treated to the non-treated population of cells.

2.2.7. Assessment of mitochondrial superoxide radical ($^{\bullet}O_2^-$) generation

Cells were seeded in 96 flat bottom well plates in 0.1 mL volume (100 000 cells/mL) and left overnight to settle. On the next day, investigated compounds were added in a 0.05 mL volume up to final concentrations of 50 μM per well. Cells treated with 0.5% DMSO were used as negative controls. After 6^{h} of incubation, cells were detached by trypsin treatment and stained with MitoSox Red (ThermoFisher Scientific; cat. no. M36008) according to the manufacturer's instructions. The analysis was performed on Guava® easyCyte 12HT Benchtop flow microcapillary cytometer. Pro-oxidant activity is analyzed over the percentage of cells positive for $^{\bullet}O_2^-$ and over the mean fluorescent intensity (MFI) expressed in arbitrary

units (AU). MFI parameter is computed for $^{\bullet}O_2^-$-positive subpopulation and corresponds to the mean flow of $^{\bullet}O_2^-$ per cell. Statistical comparison of MFI values was performed using the Kruskal-Wallis test with an unpaired *t*-test with Welch's correction as a post-test.

2.2.8. Assessment of anti-migratory activity

Cells were seeded in 96 flat bottom well plates (Corning® Costar®; cat. no. CLS3596) in 0.1 mL volume (100 000 cells/mL) using a complete DMEM medium. Cells were kept for an additional few days to form a confluent layer with medium exchanged daily. When confluency had been reached, a complete medium was exchanged with FBS-free DMEM and left on cells for 18^h. After that, a scratch in a cell layer was made using 0.2 mL pipette tips; cells were gently washed twice with serum-free medium, stained with Calcein AM, and imaged on Celigo® cytometer. The medium was then discarded and replaced with a solution of investigated compounds (1, 10, and 30 μM, final concentrations) prepared in DMEM supplemented with 1% FBS. After 24^h incubation, cells were stained with Calcein AM, and images were taken on Celigo®. Changes in the size of the scratched area between 0 and 24^h of treatment were analyzed using TScratch software (Computational Science, ETH Zurich, CLT Switzerland). Results are expressed as % of open wound area at 24^h, while statistical significance was determined using the Kruskal-Wallis test and unpaired *t*-test with Welch's correction.

2.2.9. Determination of antimicrobial activity

Antimicrobial activity was tested against a panel of microorganisms including three Gram-negative bacteria *Escherichia coli* (ATCC 25922), *Proteus hauseri* (ATCC 13315), *Klebsiella pneumoniae* (ATCC 10031), three Gram-positive bacteria *Staphylococcus aureus* (ATCC 6538), *Bacillus subtilis* (ATCC 6633), *Clostridium sporogenes* (ATCC 19404), yeasts *Candida albicans* (ATCC 10231), *Saccharomyces cerevisiae* (ATCC 9763), and fungal strain *Aspergillus brasilliensis* (ATCC 16404).

Antimicrobial activity was evaluated using the broth microdilution method, according to NCCLS [14]. The 96-well plates were prepared by dispensing 100 μL of Mueller–Hinton broth for bacteria and Sabouraud dextrose broth for yeasts and fungi, into each well. A 100 μL aliquot from the tested compounds' stock solution (concentration 10 mg/mL in DMSO) was added into the first row of the plate and double diluted by using a multichannel pipette. The suspensions of bacteria, yeasts, and fungi were prepared in sterile 0.9% saline. Suspension turbidity evaluation was conducted by comparison with 0.5 McFarland's standard.

A 10 μL of diluted bacterial, yeast, or spore suspension was added to each well to give a final concentration of 5×10^5 CFU/mL for bacteria and 5×10^3 CFU/mL for fungi and yeast. Chloramphenicol served as a positive control for bacteria, while amphotericin B was a positive control for yeasts and fungi.

The inoculated plates were incubated at 37ºC for 24^h for bacteria, and at 28ºC for 48^h for the yeasts and fungi. The bacterial growth was visualized by adding 20 μL of 0.5% 2,3,5-triphenyltetrazolium chloride (TTC) aqueous solution [15]. Minimum inhibitory concentration (MIC) was defined as the lowest concentration of the compounds that inhibited bacterial growth (red-colored pellet at the bottom of the wells after the addition of TTC).

2.2.10. Brine shrimp assay

About 20 g of commercially purchased lyophilized eggs of *Artemia salina* was added to 0.5 L of tap water. The air was passed through the suspension by a pump under illumination for 48^h. All tested compounds were dissolved in DMSO, and various amounts (0.01–1 mg) were added to 950 μL of artificial seawater with freshly hatched nauplii. After 24^h illumination at room temperature, the number of dead and surviving nauplii was counted. Potassium dichromate served as a positive control. LC_{50} was defined as a concentration of compounds that caused the death of 50% of the nauplii. All samples were done in triplicate.

2.2.11. DPPH radical scavenging activity

The 2,2-diphenyl-1-picrylhydrazyl (DPPH) radical scavenging activity was determined by the method of Blois [16]. Commercially available free radical DPPH was dissolved in methanol at a concentration of 6.58×10^{-5} M, while tested compounds were dissolved in DMSO. Into 96-well microplate, 50 μL solutions of the tested compounds at concentrations range 0.02 to 10 mg/mL were loaded (50 μL DMSO in control). One row was used to measure the absorbance of the compounds themselves and was supplemented with 100 μL of pure methanol, while the other row was supplemented with 100 μL of DPPH solution. After incubation for 30 min at room temperature in the dark, the absorbance was measured at 517 nm. All the measurements were performed in triplicate, and the scavenging activity of the tested derivatives was calculated as:

$$\text{Scavenging activity (\%)} = (A_{control} - A_{sample} - A_0)/A_{control} \times 100,$$

Where $A_{control}$ and A_{sample} refer to the absorbance of DPPH in control solution and sample, respectively, while A_0 refers to the absorbance of the compounds solutions, because of their actual color.

The IC_{50} was defined as the antioxidant concentration necessary to decrease the amount of the initial DPPH radical by 50% and was calculated from the plotted graph of scavenging activities against the concentrations of the tested compounds. Ascorbic acid was employed as a positive control (concentrations from 50 to 500 μg mL^{-1}).

2.3. Calculations of pharmacokinetic and pharmacodynamic properties for compounds **1-5**

Molecular and ADME-Tox properties for **1-5** were calculated using pkCSM software [17]. Sites of metabolism (SoM) and the structures of putative metabolites were calculated with FAME 3 [18] and Glory [19] software, respectively. The possible biological targets for compounds **1-5** were estimated using SwissTarget software [20], [21]. All programs were used in the default settings.

3. Results and Discussion

3.1. Chemistry

The synthesis path to compounds **1-5** is given in **Scheme 3**. Michael's addition of cyclic amines (**a1-a3**) on the substituted aroylacrylic acid phenylamides gave target compounds, **1-5**. The structures of **1-5** along with the corresponding yields are shown in **Table 1** and in **Scheme 4**. The progress of the reactions was monitored using TLC. In the beginning, the equimolar amount of reactants had been used in the reaction, and if after 10^h phenylamide was still present on the TLC plate, more amine was added. As we were continually noticing the remains of phenylamide on TLC, the overall procedure changed, and we started using phenylamide/amine molar ratio of 1/1.2. This approach showed satisfactory results. The majority of the reactions proceeded smoothly at room temperature. Purification procedures varied for different compounds. After removing solvents under the reduced pressure, compounds **3** and **5** were characterized without further purification. Purification by silica gel dry flash column chromatography of all other compounds went very smoothly. The ^1H and ^{13}C NMR spectra are given in Supplementary information, **Figures S1-S5**, and the high-resolution mass spectra were given in **Figure S6**.

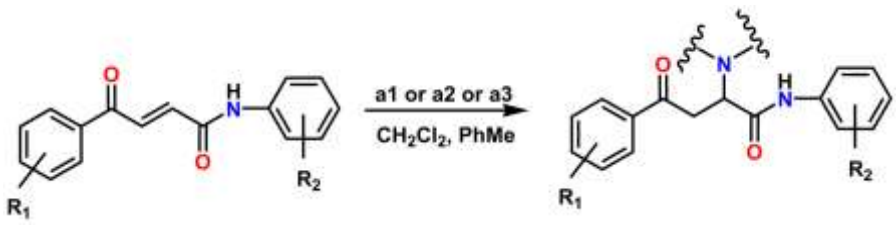

Scheme 3. Synthesis route to **1-5**. The compounds were obtained by Michael's addition of the suitably chosen substituted piperidine or piperazine fragments to the double bond of aroylacrylic acid phenylamides.

Table 1. Structures and yields of **1**-**5**.

No	R_1	R_2	R_3	Yield %
1	4- Cl	-H	a1	55
2	4- Cl	-H	a3	47
3	3,4- *di*Me	4-*i*-Pr	a3	QT
4	4-*n*-Bu	-H	a3	78
5	*β*- tetralinyl	-H	a2	QT

*QT denotes the quantitative yield.

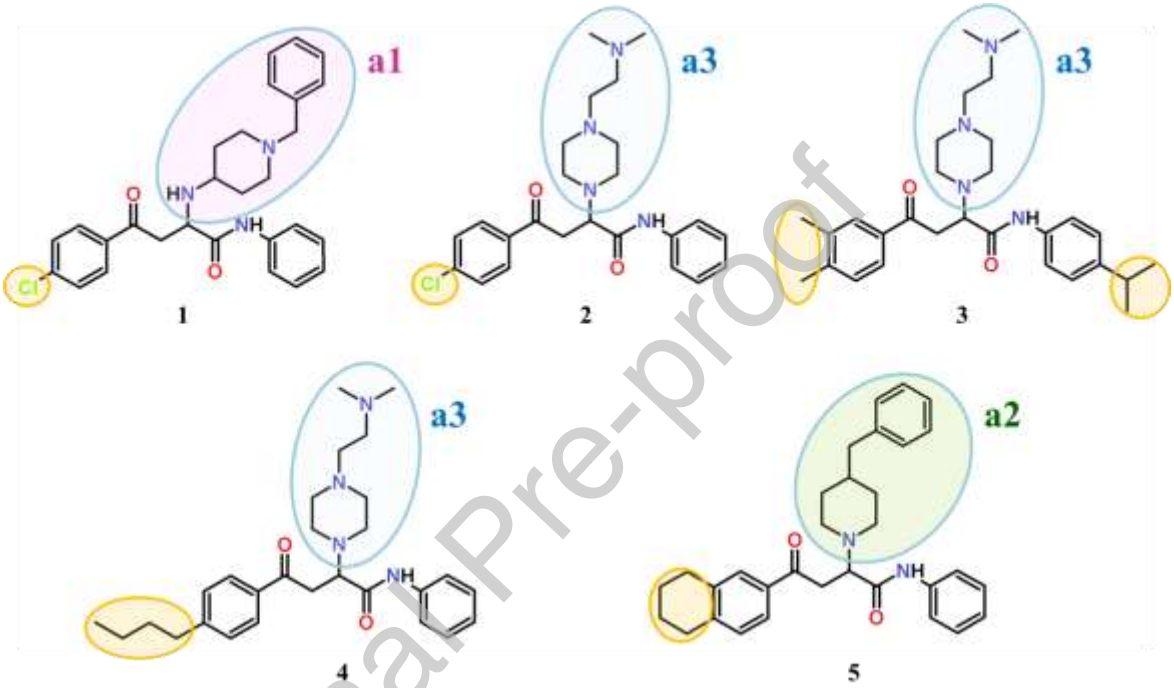

Scheme 4. Variation in the structural motifs for **1**-**5**.

3.2. Cytomic analysis of anticancer activity

3.2.1. Monitoring ability of **1**-**5** to induce death of malignant cells

Initial assessment of the ability of investigated compounds to induce malignant cell death has been performed in a cytomic manner, *i.e.*, on a panel of human cell lines of different phenotypes. The plan was to observe which cancer type may be particularly susceptible to the treatment with the compounds (**1**-**5**): a rational perspective for the organization of the following experiments. We used Calcein AM (CAM) / propidium iodide (PI) dual staining method for the evaluation of the compounds' anticancer activity which has two important advantages over the standard colorimetric cytotoxicity assays: (a) CAM/PI dual staining method may provide information on whether the tested compound restrains treated cells to

enter mitosis (inhibition of cell proliferation), or it induces cell death and (b) it allows straightaway visual discrimination between apoptotic and necrotic cell death.

After 24^h of incubation on cells, all compounds were revealed as potent inducers of cell death in all treated phenotypes (**Figures S7-S31**). With such an outcome, and to distinguish variations in response between cancer phenotypes, the modality of PI staining, rather than CAM-stained quantification, was selected. A thorough examination of the acquired images reveals that in the A549, LoVo and Skov-3 cell lines, the majority of the cells do accumulate PI with a sharply defined contour and a bright red glow, a situation typical for the formation of apoptotic bodies (**Figures S7-S11**, **S17-S21** and **S27-S31**). On the contrary, dual staining of AsPC-1 and MCF-7 cell lines yields a smudgy red glow accompanied by green coloration by CAM, resulting in a yellowish shade, typical for necrotic cell death (**Figures S12-16**, and **S22-S26**). Relying on these observations, the current investigation was further conducted on colorectal (LoVo), lung (A549), and ovarian (Skov-3) adenocarcinoma cell lines.

Quantitative assessment of death incidences in selected cell lines after treatment with compounds (**1-5**) has been performed by Annexin V/PI staining. Considering all compounds demonstrated powerful activity, the highest applied concentration in this experiment has been reduced to 75 μM, and treatments were left on cells 24^h before analysis. ~~In this experiment, investigated compounds were added in the 1- concentration range and left on cells 24^h before analysis.~~ Obtained data show that all compounds exert concentration-dependent activity, and some common patterns in responses of cell lines to applied treatments can be noticed (**Figures 1-3**). Tested compounds do not stimulate cell death in the range of 1-10 μM in any treated cell lines, while at 30 μM all of them cause a vigorous increase in double-stained events in LoVo and particularly Skov-3 cells. A549 cells reveal as the least sensitive and notable variations in the frequency of cell death are evident for **1-5** within the range from 30-75 μM. Additionally, the absence of Annexin V single-stained cells is strikingly evident in all cell lines, but when compounds were added in concentration that achieves significant activity, all or the vast majority of cells were acquired as double-stained. The events simultaneously positive for Annexin V and PI are considered as cells in the advanced phase of death, while the staining method applied here cannot precisely discriminate whether those cells are in the advanced phase of apoptosis or necrosis. To resolve whether compounds **1-5** lead cells toward necrotic or apoptotic death, plates with the remaining cells after Annexin V/PI reading were fixed in ethanol and later on primed for cell cycle analysis. The purpose of this step was to define the possible presence of DNA fragmentation in the treated samples that can be seen as

Sub-G0/G1 accumulation and serves as a confirmation that cells have undergone apoptotic death [22]. As presented in **Supplementary figures S32-S34**, percentages of events at the Sub-G0/G1 strongly correlate with percentages of double-stained cells in **Figures 1-3.** This result demonstrates that almost all cells found in an advanced phase of death were actually in the late stage of apoptosis. According to concentration-response curves (**Supplementary figure S35**) and computed CdC_{50} values (**Table 2**), compound **4** is the most effective in all three cell lines, followed by compound **2** which reveals high activity in Skov-3 cells. Compounds **2** and **5** score similar CdC_{50} in A549 cells, and all compounds except **4**, had similar CdC_{50} values in LoVo cell line. Compound **1** is the least potent in all cell lines, but still able to arouse cell death in all treated cells.

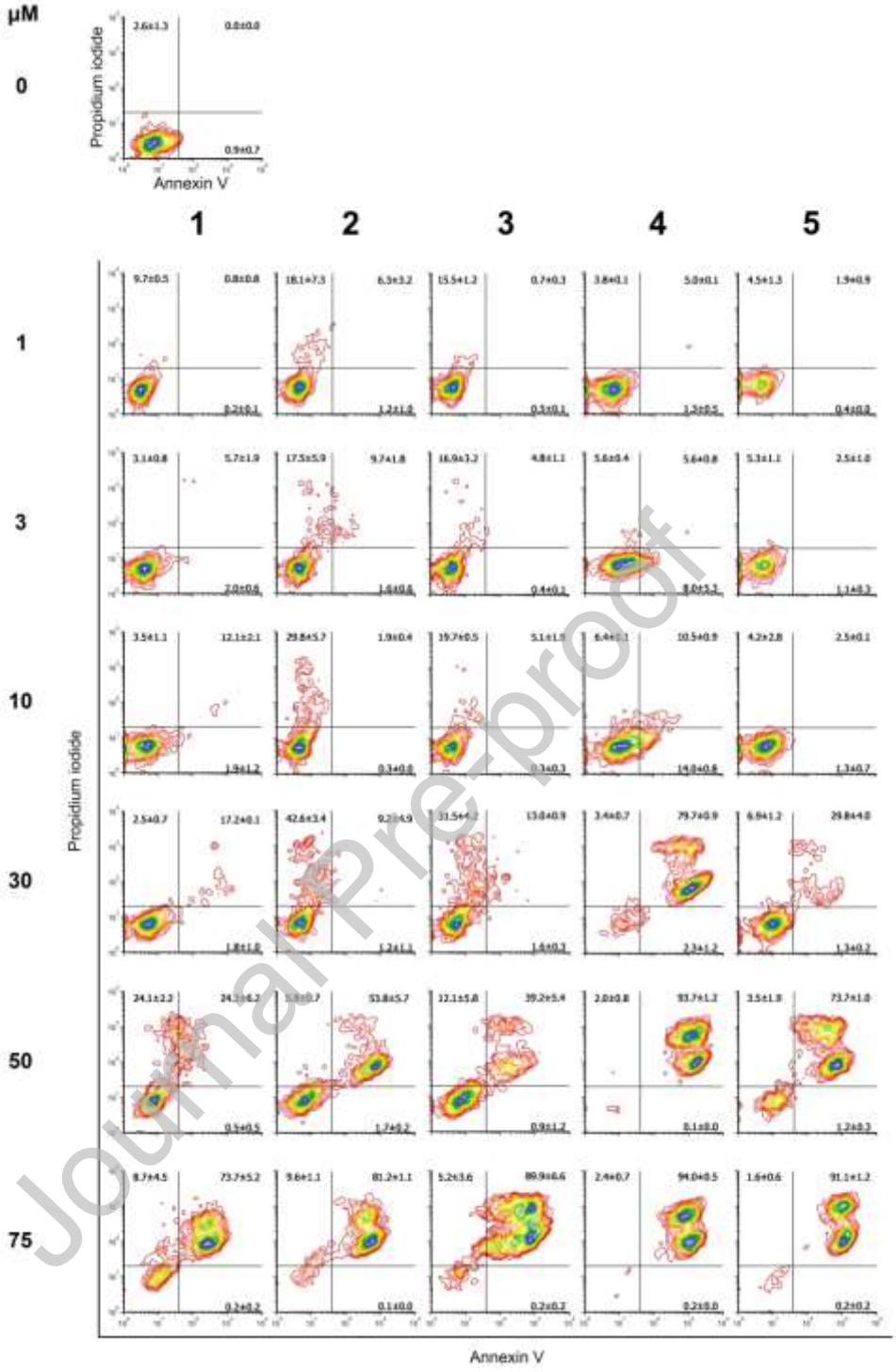

Figure 1. Representative figures of Annexin V/propidium iodide dual staining after 24[h] incubation of A549 cells with compounds **1**-**5**. In Annexin V/PI dot plots cells are discriminated as viable (non-stained cells, lower left quadrant), cells in the early phase of apoptotic death (Annexin V single-stained cells, lower right quadrant), cells in advanced phases of cell death (double-stained cells, upper right quadrant), and cells in early necrosis (PI single-stained cells, upper left quadrant). Results are represented as the mean ± SD percentages of two replicates from independent experiments.

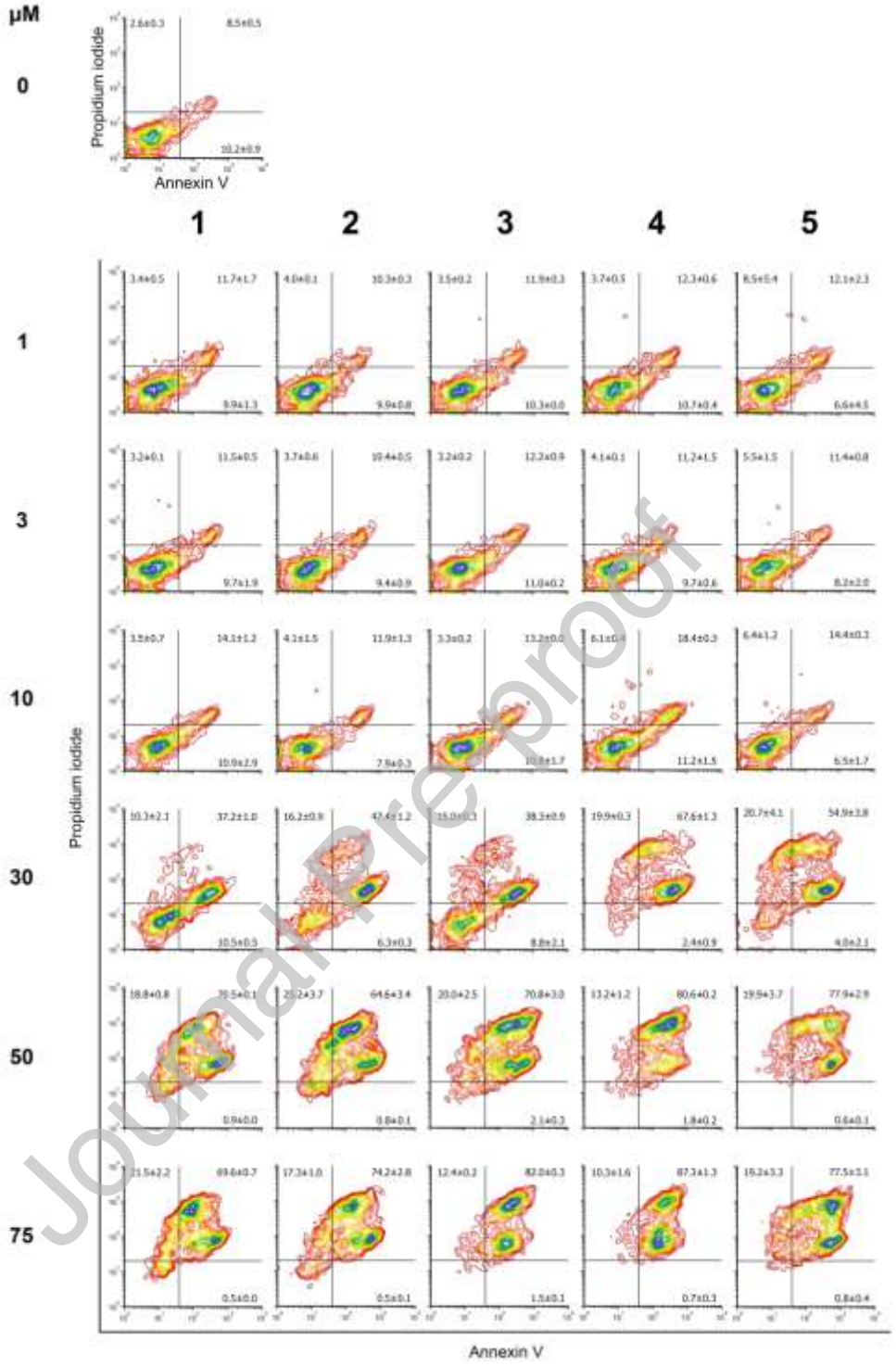

Figure 2. Representative figures of Annexin V/propidium iodide dual staining after 24[h] incubation of LoVo cells with compounds **1**-**5**. In Annexin V/PI dot plots cells are discriminated as viable (non-stained cells, lower left quadrant), cells in the early phase of apoptotic death (Annexin V single-stained cells, lower right quadrant), cells in advanced phases of cell death (double-stained cells, upper right quadrant), and cells in early necrosis (PI single-stained cells, upper left quadrant). Results are represented as the mean ± SD percentages of two replicates from independent experiments.

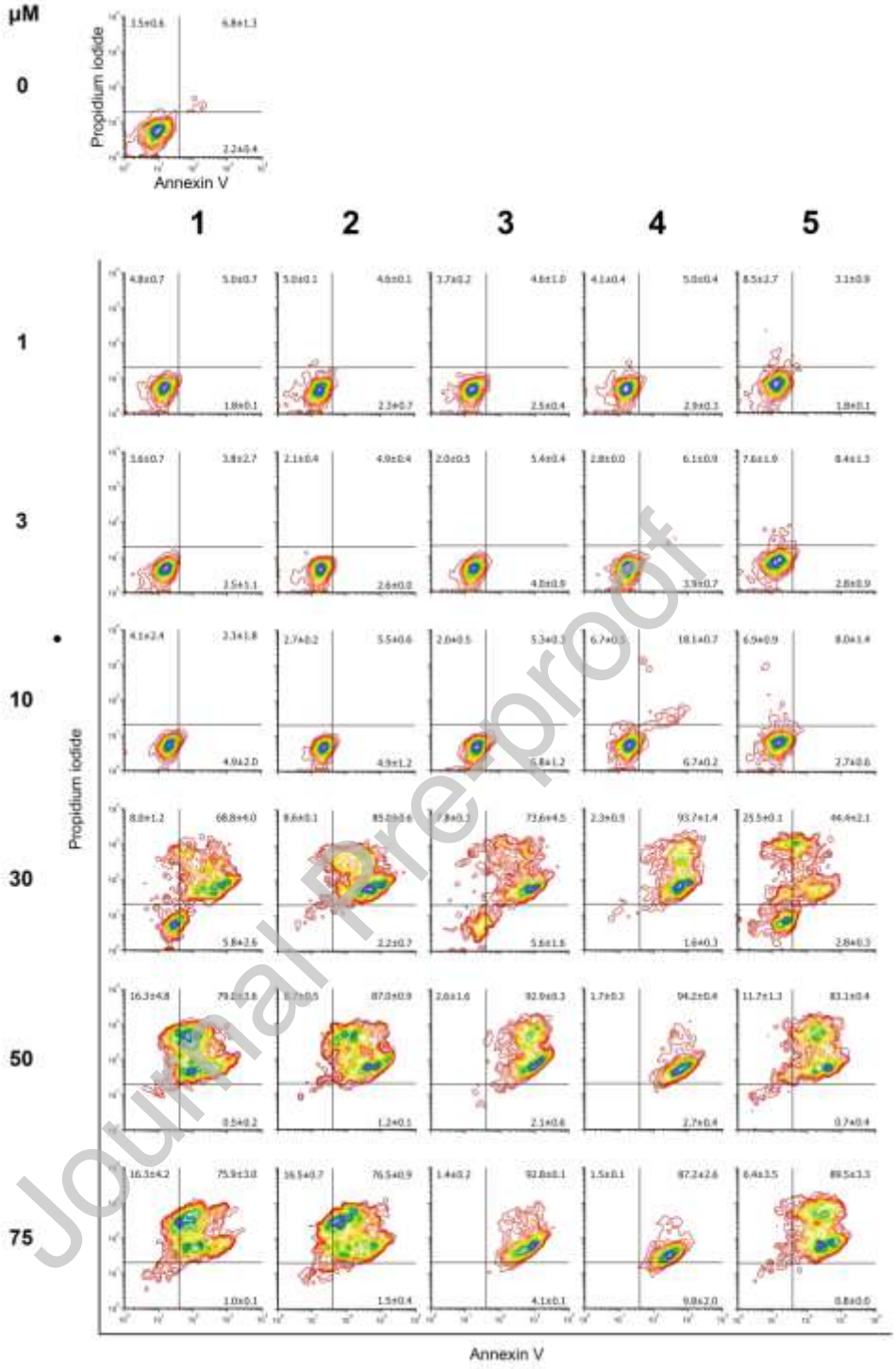

Figure 3. Representative figures of Annexin V/propidium iodide dual staining after 24[h] incubation of Skov-3 cells with compounds **1**-**5**. In Annexin V/PI dot plots cells are discriminated as viable (non-stained cells, lower left quadrant), cells in the early phase of apoptotic death (Annexin V single-stained cells, lower right quadrant), cells in advanced phases of cell death (double-stained cells, upper right quadrant), and cells in early necrosis (PI single-stained cells, upper left quadrant). Results are represented as the mean ± SD percentages of two replicates from independent experiments.

Table 2. Concentrations of investigated compounds that induce death in 50% of treated cells after 24^h of treatment were computed from data acquired by Annexin V/PI staining. Values are expressed as the mean ± standard deviation of two replicates from independent experiments.

	A549 cells	**LoVo cells**	**Skov-3 cells**
Compound	**CdC_{50}[1] [μM]**	**CdC_{50} [μM]**	**CdC_{50} [μM]**
1	51 ± 4	26.1 ± 0.3	25 ± 2
2	33 ± 4	25.1 ± 0.3	13 ± 2
3	41 ± 1	26 ± 1	22 ± 2
4	17 ± 1	12.7 ± 0.2	12.9 ± 0.1
5	34.6 ± 0.3	24 ± 1	21 ± 6

[1]CdC_{50} - cell death concentration represents the one that induces death in 50% of treated cells.

3.2.2. Cell cycle analysis

Next, we wanted to determine which phase of cell division is affected by compounds **1**-**5**. Considering that cell survival was less than 10% in the majority of samples subjected to tested compounds at concentrations of 50 and 75 μM for 24^h, incubation time in this experiment has been reduced to 12^h. Variations in cell cycle distribution between cell lines subjected to the same compound are ordinary and may be attributed to the differently compromised activity of one or more mitotic checkpoints [23]. As is represented in **Figure 4**, a common feature in all acquired samples is an elevated percentage of events at the S phase compared to control, which indicates that treated cells are suffering obstacles during the DNA replication process. However, accumulation at the S phase as an isolated development is found at lower concentrations of our compounds. With increasing concentrations, cell cycle distribution evolves toward arrest at the G1-to-S checkpoint in A549 and LoVo cells and even to arrest at the S-to-G2 transition point in Skov-3 cells subjected to compounds **3** and **5**. At this point, it is impossible to assume how our compounds interfere with the course of division during the S phase, *i.e.*, whether they provoke DNA damage or are hindering the activity of machinery that controls duplication of chromosomal material.

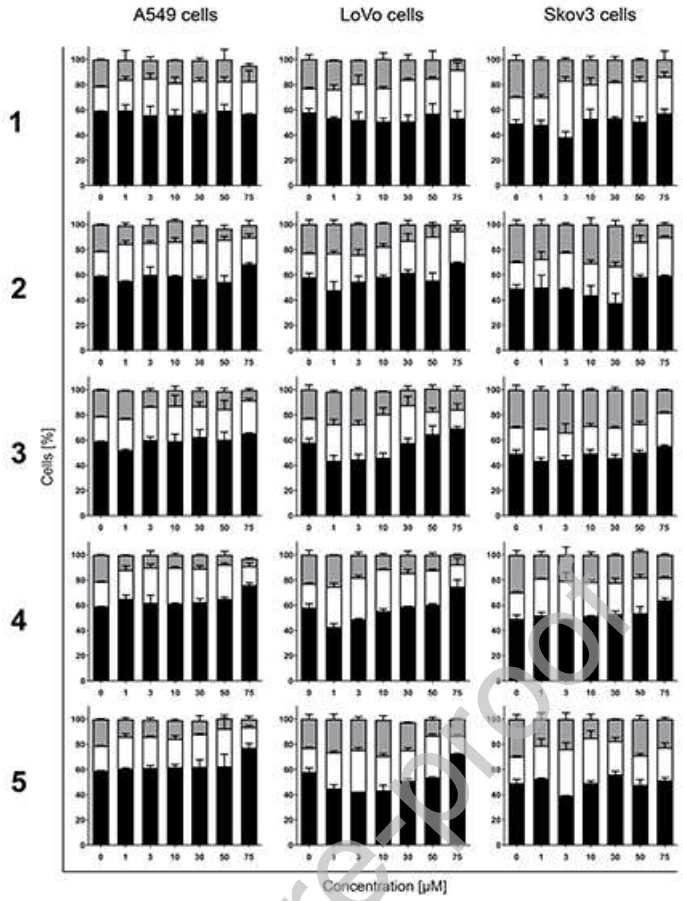

Figure 4. Distribution of cells at the G0/G1 phase (black bars), S phase (white bars), and G2/M phase (gray bars) after 12^h treatment with **1**-**5**, with respect to non-treated control population. Results are expressed as the mean ± SD percentages of two replicates from independent experiments.

3.2.3. Assessment of mitochondrial superoxide radical ($^{\bullet}O_2^-$) generation

There is a large body of evidence that chemotherapeutic agents may cause DNA damage by the generation of reactive oxygen species (ROS) [24],[25]. Mitochondria are the main source of ROS, where $^{\bullet}O_2^-$ is the primary ROS formed in this organelle [26], [27]. Considering that cell cycle changes assayed after 12^h of treatment indicate that cells experience a particular type of drawback over the DNA replication phase, the assessment of whether our compounds can stimulate mitochondrial $^{\bullet}O_2^-$ production was tested. Among treated phenotypes, A549, and particularly LoVo cells have low expression of manganese superoxide dismutase (MnSOD) [28],[29]. MnSOD is a mitochondrial enzyme responsible for the conversion of $^{\bullet}O_2^-$ to membrane-permeable hydrogen peroxide (H_2O_2) and represents the first line of defense for oxidative respiratory chain and sustainable production of ATP. If the extent of created $^{\bullet}O_2^-$ is overwhelming, or MnSOD fails to efficiently dismute them to H_2O_2, $^{\bullet}O_2^-$ will be exported *via* voltage-dependent anion channels into the cytosol where further can

be converted either to H_2O_2 or to highly reactive hydroxyl radicals ($^{\bullet}OH$) [30] . Contrary to H_2O_2 which is involved in many physiological processes, $^{\bullet}OH$ is the most reactive ROS interacting with different cellular components. Reactive intermediates that arise as a result of lipid oxidation by $^{\bullet}OH$, damage DNA by attacking either bases or DNA backbone [31]. Incubation time in ROS experiment was reduced to 6^h to detect if the generation of $^{\bullet}O_2^-$ may be the event responsible for a series of sequences over another 18^h of treatment, while the chosen concentration (50 μM) is the lowest one corresponding to significant percentage of cell death that each of compound induced at 24^h in every treated cell line (**Figures 1-3**). Along with the percentage of $^{\bullet}O_2^-$-generating cells, acquired data were analyzed for mean fluorescent intensity (MFI) computed for ROS-positive subpopulation, thus providing information on the arbitrary flux of existing $^{\bullet}O_2^-$ per cell.

The percentage of cells positive for increased $^{\bullet}O_2^-$ production after 6^h of treatment with **1**-**5** are given in the Supplementary material (**Figure S36**), while MFI values are given in **Table 3**. Considering the extent of ROS-positive subpopulations, LoVo cells are most affected with negligible differences between samples treated with **1**-**5**. In A549 and Skov-3 cells, compound **4** provokes prooxidative stress for the maximum percentage of cells, while **5** proves to be the least harmful. There are no meaningful variations in the percentage of $^{\bullet}O_2^-$-generating A549 cells subjected to **1**, **2**, or **3**. In Skov-3 cells, activity from **1** to **3** is decreasing, respectively. Nevertheless, the analysis of MFI values affords an entirely new perspective on the compounds capability to initiate emerging of ROS (**Table 3**). Firstly, **4** is the only compound that, for each cell phenotype, triggers the formation of $^{\bullet}O_2^-$ at such a rapid pace that it results in statistical significance compared to the non-treated control. In A549 and LoVo cells, **4** and **2** record the highest MFI values with respect to other compounds, but in Skov-3 cells, **4** remains the one causing the profuse amount of $^{\bullet}O_2^-$ per cell. Since Skov-3 cells are described with high expression of MnSOD [29], the incompetency of their mitochondrial antioxidant defense to convert $^{\bullet}O_2^-$ to H_2O_2 should not be addressed as an issue. Additionally, compound **4** induces trivial incidence of necrotic events in Skov-3 cells at 24^h (**Figure 3**), which is particularly impressive considering it would be expected that $^{\bullet}O_2^-$ production of this magnitude would quickly disrupt electron transport chain and oxidative phosphorylation, with a consequently substantial decrease in ATP levels that are necessary to complete the process of apoptotic death. Secondly, MFI values for compound **5** in LoVo and Skov-3 cells are at the level of non-treated controls but elevated in A549 cells. As noted above, LoVo and A549 cells are shown to have poorly expressed MnSOD [28], [29], which, together with the current results, indicates that the mechanism of $^{\bullet}O_2^-$ outflow generated by **5**

is diverse between these cell lines. One of the possible explanations is that **5** undergoes intracellular phases 1 and 2 metabolism before interaction with mitochondrial proteins, while yielded end product(s) can have different structures and features due to significant heterogeneity in expression and activity of drug-metabolizing enzymes among tumor types [32], [33]. More advanced studies will be necessary to define the exact metabolic transformation of here investigated compounds once they enter the cell, thus variations in their activities can be precisely explained. Finally, in terms of described cell cycle changes, it is highly possible that ROS play a significant role in the initiation and/or transduction of apoptotic signaling in LoVo and A549 cells subjected to any of the tested compounds, as well as in Skov-3 cells treated with the compound **4**.

Table 3. Mean fluorescence intensity (MFI) expressed in arbitrary units, computed for $^{\bullet}O_2^-$ positive subpopulation. Numbers represent the mean ± standard deviation of three replicates.

Compound	A549 cells	LoVo cells	Skov-3 cells
Non-treated	149 ± 4	339 ± 14	238 ± 51
1	683 ± 23**[1]	636 ± 26**	333 ± 26
2	856 ± 80**	802 ± 16**	350 ± 11
3	653 ± 32**	678 ± 34**	337 ± 31
4	764 ± 24**	713 ± 9**	878 ± 1***
5	440 ± 15*	428 ± 30	192 ± 21

[1]Statistical significance was computed using the Kruskal-Wallis test with unpaired *t*-test with Welch's correction as post-test comparing results of treated and correspondingly non-treated samples: *p<0.05; **p<0.01; ***p<0.001.

3.2.4. Determination of cellular activated caspase-8 and/or caspase-9

To afford additional perspective regarding intracellular developments coinciding with $^{\bullet}O_2^-$ generation, patterns of intrinsic and extrinsic apoptotic pathways activation were monitored after 6^h of treatment, with compounds added at the same concentration as in ROS experiment. As given in **Figure 5,** activation of caspase-9, *i.e.*, intrinsic apoptotic pathway, is the leading event in almost all acquired samples. This result reveals that treated cells have been suffering from severe homeostasis distress, which can be related to extensive ROS production [34], while other possible causes cannot be excluded. Although MFI values for **1**-**3** and **5** in Skov-3 cells were at the control level, the impact of possibly elevated H_2O_2 and its role in redox signaling was not evaluated in this study and deserves further examination [35]. Besides, a statistically significant decrease in activated caspase-8 compared to non-treated controls is found in all cells treated with **4**, as well as in LoVo samples subjected to **1** and **2**.

Considering the short incubation time, this effect can hardly be addressed to the down-regulated expression of procaspase-8. Further investigations should be directed toward the possible influence of compounds **1-5** on the conversion of procaspase-8 to its active form and the activity of regulators involved in this process [35]. Also, compound **5** in Skov-3 cells activates caspase-8 independently of caspase-9 (**Figure 5**), indicating its ability to serve as a dual-targeting agent in specific tumor phenotypes. This duality in the activity of **5** is observed in the same cells where it caused the negligible generation of mitochondrial $^{\bullet}O_2^-$, thus it may be possible that this feature was concealed in A549 and LoVo cell lines due to significant oxidative stress and promptly initiated apoptotic death by capsase-9.

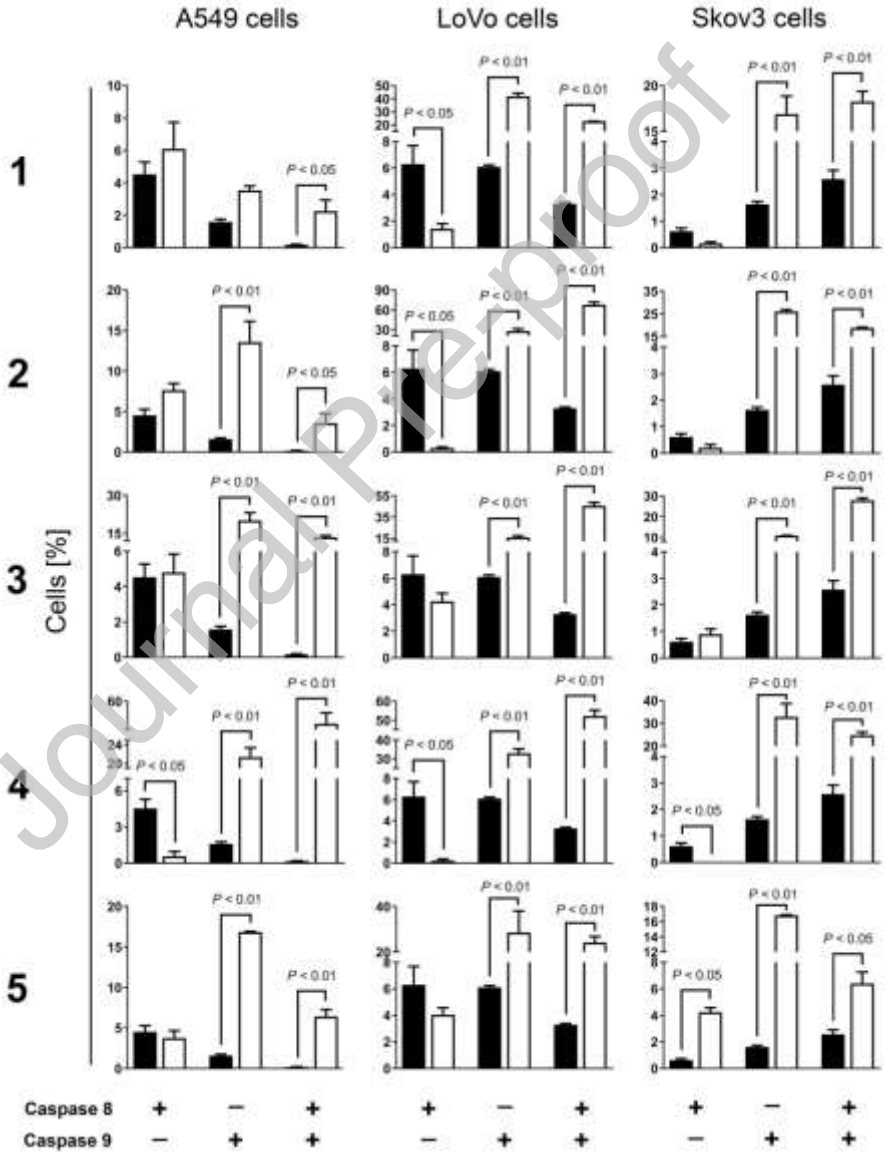

Figure 5. Percentages of cells with activated caspase-8, caspase-9, or both, determined after 6^h incubation with **1-5**. Results are represented as the mean ± SD of three replicates from independent experiments. The statistical evaluation has been performed using an unpaired *t*-test with Welch's correction comparing treated (open bars) to non-treated populations (closed bars).

3.2.5. Assessment of anti-migratory activity

Aside from pro-apoptotic activity, cancer cell mobility was examined, as it has a vital role in cancer dissemination. For that purpose, the wound-healing assay has been performed in Skov-3 cells, known to possess highly expressed migratory and invasive properties [36]. After 24^h, 84 ± 5% of the initial wound area remains uncovered in non-treated samples, while each of the investigated compounds affects cell migration to a different extent (**Figure 6**). Except for **5**, a negative correlation between inhibition of cell mobility and tested concentration is obtained for all other compounds (**Figure 6**). While **3** has the least influence, whether it is added at 1, 10, or 30 μM, **2** and **4** achieve statistically significant inhibition of cell migration at 1 and 10 μM but have no effect at 30 μM. Moreover, compound **1** significantly stimulates cellular mobility at 30 μM. Thus, in those samples cells covered 30 ± 2% of starting wound surface. Therefore, the most efficient compound **5** achieves statistically significant repression of cellular migratory ability at each of three tested concentrations.

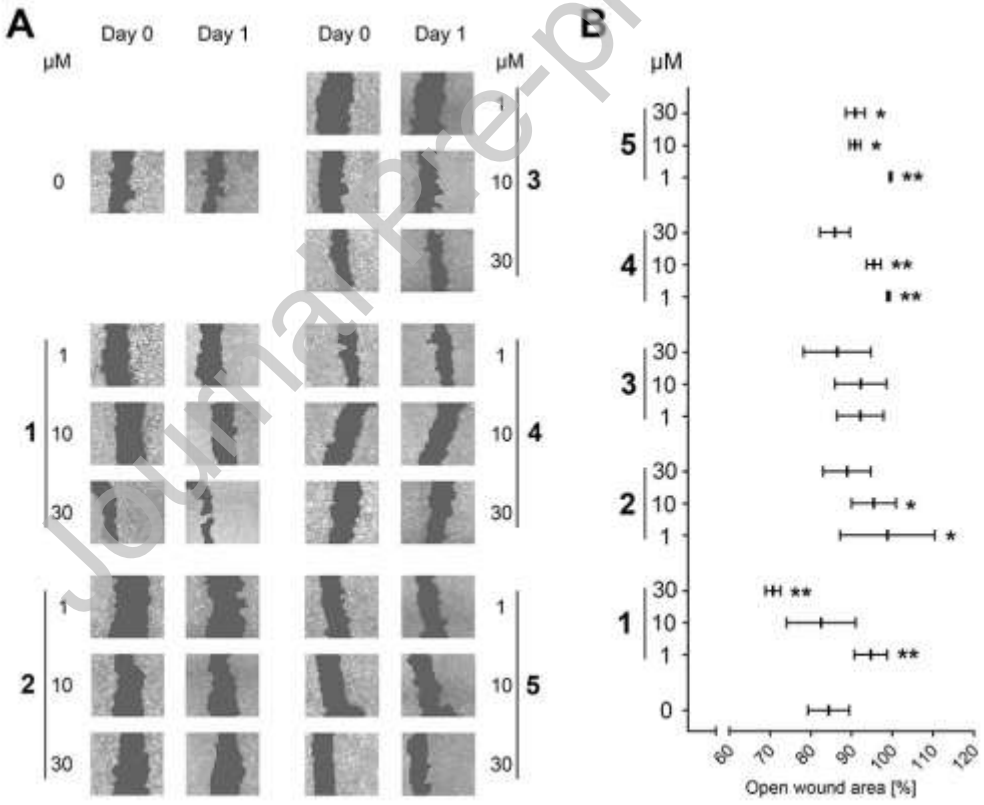

Figure 6. Impact of investigated compounds on cell motility evaluated by wound healing assay. **(A)** Representative images of scratch assay acquired by Celigo imaging cytometer after cells were stained with Calcein AM. Images were taken just before the addition of compounds **1**-**5** (Day 0) and 24^h later (Day 1). **(B)** Mean ± SD plot of open wound area after treatment with compounds **1**-**5**, determined by TScratch software analysis of images acquired at 0 and 24^h. Statistical significance was tested using the Kruskal-Wallis test and unpaired *t*-test with Welch's correction.

3.3. Antimicrobial activity

Given the significant cytotoxicity of the **1-5** toward malignant cells, antimicrobial activity of the compounds against several bacterial and fungal strains was determined. The results of these experiments are given in **Tables 4** and **5**. Compounds **1** and **4** exerted significant antibacterial activity and were one order of magnitude more potent than chloramphenicol in almost all investigated bacterial strains except for *S. aureus* and *B. subtilis*. Compound **3** was more active toward *E. coli* and *C. sporogenes* strains than chloramphenicol and was moderately potent toward other bacterial strains. Compounds **2** and **5** did not exhibit significant antimicrobial activity in all investigated bacterial strains.

Regarding antifungal activity, all compounds were significantly less potent than amphotericin B. The only exception is **1** that revealed four-fold higher antifungal activity toward *A. brasiliensis* than amphotericin B.

Table 4. The antibacterial activity of the compounds.

Strain	MIC (mM)					
	1	**2**	**3**	**4**	**5**	**Chloramphenicol**
E. coli	0.083	44.019	0.082	0.046	1.30	0.192
P. hauseri	0.042	22.010	0.656	0.186	1.30	0.387
K. pneumoniae	0.042	11.005	0.328	0.186	1.30	0.192
S. aureus	0.332	44.019	0.656	0.372	1.30	0.046
C. sporogenes	0.166	22.010	0.328	0.093	1.30	0.774
B. subtilis	0.166	11.005	0.656	0.186	1.30	0.046

Table 5. The antifungal activity of the compounds.

Strain	MIC (mM)					
	1	**2**	**3**	**4**	**5**	**Amphotericin B**
S. cerevisiae	0.084	44.019	0.332	0.186	0.650	0.01
C. albicans	0.084	176.076	0.166	0.186	0.650	0.02
A. brasiliensis	0.011	5.503	0.332	0.372	0.650	0.04

3.4. Acute toxicity towards *Artemia salina* and antioxidant activity

The main disadvantage of drugs for anticancer treatment is their narrow therapeutic index, meaning a tight window between the dose required for desirable therapeutic effect and the dose that induces serious side effects [37], [38]. A large scale of preclinical *in vivo* testing and clinical trials are necessary to thoroughly study the pharmacokinetic properties and

toxicity profile of a new drug. Therefore, at the early stage of *in vitro* investigation it is impossible to define the most appropriate cellular model that can provide valid information on what adverse events the tested drug may cause. For that reason, instead to apply our compounds on monolayer culture of immortalized cells cloned from healthy tissue, we decided to run the test on *Artemia salina* (brine shrimp), which are eukaryotic organisms widely used for the first-line toxicity screenings [39], [40], [41], [42]. Considering a highly potent prooxidative activity of **4**, it was not surprising that this compound reduced the survival of brine shrimps for a half at a twice lower concentration than potassium-dichromate that served as the positive control (**Table 5**). However, it was not expected of compound **1** to demonstrate stronger toxic activity than **4**, as well as in comparison to all other tested compounds. Although **2**, **3**, and **5** also induced the death of treated organisms, their LC_{50} concentrations were 2.8, 3.6, and 2.4-fold higher compared to positive control. Therefore, ROS production that is found as a possible triggering mechanism of apoptotic death in malignant cell cultures may not necessarily cause toxic effects on healthy tissues or model organisms. This result accentuates uncertainty of extrapolation of toxicity data from cell to organism models, and affirms the necessity to define the accurate course of metabolic transformation, distribution and possible accumulation in peripheral body compartments for reliable evaluation of short-term and long-term side effects. Comprehensive toxicological analysis on non-malignant cell lines are going to be performed in future investigations.

Regarding antioxidant activity estimated by DPPH assay, compounds **1** and **5** show no antioxidative activity at all, while compounds **2**, **3** and **4**, show very weak activity, around three orders of magnitude lower than the vitamin C. This was expected as the structures of the compounds do not possess particular structural features typical of compounds with antioxidative activity.

Table 6. Acute toxicity toward *Artemia salina* and antioxidant activity of the compounds.

Compound	Brine shrimp LC_{50} (mM)	DPPH test, LC_{50} (mM)
1	0.017±0.009	/
2	0.217±0.033	9.168±0.095
3	0.279±0.043	4.581±0.058
4	0.035±0.011	7.324±0.092
5	0.182±0.028	/
$K_2Cr_2O_7$	0.077±0.016	/
Ascorbic acid	/	0.079±0.012

3.5. Theoretical estimation of pharmacokinetic (ADME-Tox) and pharmacodynamic properties

Further examination of the pharmacokinetic and pharmacodynamic properties of the compounds **1-5** was estimated using several on-line available software tools: (a) pkCSM software for the calculation of molecular properties and various properties related to the administration, distribution, metabolism and elimination of the compound as well as their toxicity [17]; (b) FAME 3 and Glory software tools for estimation of the sites of the metabolism of the compounds and the structures of the putative metabolites [18],[19]; and (c) Swiss Target was used for the estimation of the possible biological targets for the compounds **1-5** [20],[21].

3.5.1. Estimation of ADME-Tox calculations by pkCSM software for **1-5**

The results of the drug-like and ADME-Tox properties calculated using the pkCSM on-line software tool were summarized in **Table 7**. According to the calculated molecular properties represented in the first panel of **Table 7**, it is evident that compounds **2-4** meet the Lipinski rule of five (MW < 500 g/mol, logP < 5, HBD < 5 and HBA < 10) [43], as a guideline for the good oral bioavailability. Compound **1** has estimated logP slightly above 5, while compound **5** has a significantly higher value of logP and therefore does not meet the Lipinski criterion. The estimated absorption parameters for the compounds are given in the second panel of **Table 7**. According to the model based on human epithelial colorectal adenocarcinoma cells (CaCo-2) the compounds have high predicted values of permeability through intestinal membranes, especially compounds **2** and **3**. In accordance with this estimation, the % of the intestinal absorption of the compounds is exceptionally high, above 88%. However, all compounds are not good candidates for transdermal delivery route according to the model, since they have low estimated skin permeability below -2.5. All the compounds were estimated to be both substrate and inhibitor for P-glycoprotein transporter.

The distribution parameters for compounds **1-5** are given in the third panel of **Table 7**. Interestingly, all the compounds showed an exceptionally high volume of distribution (VDss) as an indication of the higher presence of the compounds in the tissues than in plasma. However, the contradictory estimation was low Fu (fraction unbound) value, which indicates very high binding of the compounds to plasma proteins. Both models for central nervous system (CNS) and blood brain barrier (BBB) permeability predicted poor entrance and distribution of the compounds in the central nervous system.

Regarding the metabolic transformation of the compounds (fourth panel of **Table 7**), it was estimated that **1-5** may interact with CYP3A4 both as a substrate as well as an inhibitor, while it was estimated that they are rather inhibitors of CYP2D6 isoform of the enzyme. For the majority of the compounds, it was found that they may not interact with other cytochrome isoforms such as CYP1A2, CYP2C9, and CYP1A2. Regarding excretion, the software estimated that compounds **3**, **4** and **5** might be substrates for renal organic cation transporter, so their renal route of elimination is probable.

Toxicological properties of the **1-5** are given in the last panel of **Table 7**. The software predicted that compounds aren't mutagenic and also calculated moderate maximal tolerated doses for humans, with the highest (the least toxic) being 1.99 mg/kg/day for compound **1**. Other estimated toxic properties were unfavorable, for instance, all compounds were estimated to be hepatotoxic and to inhibit hERG II channels (the Human Ether-a-go-go-related Gene Potassium Channel), which indicates that they might cause fatal ventricular arrhythmia (a common cause of the failure in the drug development), probably due to the presence of the piperidine moiety in the structure, which is a common structural motif of the well-known hERG II inhibitors. The toxicity was estimated for the two model organisms *T. pyriformis* (protozoal bacteria) and flathead minnows (fish). The compounds were estimated as highly toxic toward *T. pyriformis*, since their estimated $pIGC_{50}$ values were considerably higher than -0.5. However, estimation of toxicity toward flathead minnows supposed that all the compounds are mostly non-toxic since they had values of $logLC_{50}$ fairly higher than -0.3. Oral rat acute toxicity was unrealistically low and probably falsely predicted.

Table 7. Estimated ADME-Tox properties by pkCSM software.

	Property	Compound				
		1	**2**	**3**	**4**	**5**
Descriptors	**Molecular Weight**	476.02	473.061	478.681	494.742	480.652
	LogP	5.1743	4.1255	4.1861	4.8147	6.1002
	Rotable Bonds	9	9	10	12	8
	HB Acceptors	4	5	5	5	3
	HB Donors	2	1	1	1	1
	Surface area	205.675	203.053	210.839	218.210	214.276
Absorption	**Water solubility, mmol/L**	38.5	50.9	472.10	363.078	73.960
	Caco2 permeability, log Papp in 10^{-6} cm/s	1.223	1.381	1.749	1.132	1.230
	Intestinal absorption, Hu, %	88.826	92.612	88.019	88.922	89.649
	Skin permeability, log Kp	-2.736	-2.739	-2.738	-2.737	-2.735
	P-glycoprotein substrate	Yes	Yes	Yes	Yes	Yes
	P-glycoprotein I inhibitor	Yes	Yes	Yes	Yes	Yes
	P-glycoprotein II inhibitor	Yes	No	Yes	Yes	Yes

Distribution	**VDss (human), log L/kg**	1.268	1.941	1.656	1.712	0.47
	Fraction unbound, Fu	0	0.138	0.281	0.265	0.037
	BBB permeability, log BB	0.117	0.087	0.144	0.114	-0.026
	CNS permeability, log PS	-1.997	-2.414	-2.434	-2.526	-1.604
Metabolism	**CYP2D6 substrate**	Yes	No	No	No	No
	CYP3A4 substrate	Yes	Yes	Yes	Yes	Yes
	CYP1A2 inhibitor	Yes	No	No	No	No
	CYP2C19 inhibitor	No	No	Yes	No	Yes
	CYP2C9 inhibitor	No	No	No	No	No
	CYP2D6 inhibitor	Yes	No	Yes	Yes	Yes
	CYP3A4 inhibitor	Yes	Yes	Yes	Yes	Yes
Excr.	**Total Clearance, log mL/min/kg**	1.068	0.798	0.955	1.197	1.011
	Renal OCT2 substrate	No	No	Yes	Yes	Yes
Toxicity	**AMES Toxicity**	No	No	No	No	No
	Max. tolerated dose, mg/kg/day, Hu	1.99	0.504	0.267	0.204	0.372
	hERG I inhibitor	No	No	No	No	Yes
	hERG II inhibitor	Yes	Yes	Yes	Yes	Yes
	Oral Rat Acute Toxicity, LD_{50}, mol/kg	2.648	2.993	2.721	2.760	2.479
	Oral Rat Chronic Toxicity, log mg/kg/day	1.504	1.07	2.845	2.732	1.217
	Hepatotoxicity	Yes	No	Yes	Yes	Yes
	Skin sensitisation	No	No	No	No	No
	T. Pyriformis toxicity, log μg/L	0.308	0.368	0.285	0.285	0.285
	Minnow toxicity, log mM	1.944	4.711	0.139	-0.355	-0.514

3.5.2. The sites of metabolism (SoMs) and metabolites' estimation by FAME 3 and Glory software for **1-5**

The sites of metabolism (the atom position in the molecule at which metabolic reactions are initiated, SoM) of **1-5** were predicted by FAME 3 software and the structure of metabolites was estimated by Glory. There are many predictors of SoM available, but most are limited to cytochrome P450 (CYP) mediated metabolism. FAME 3 is the third generation of machine learning models for the prediction of SoM and is trained on a new, comprehensive data set of drug-like molecules annotated with SoMs originating from the MetaQSAR database. FAME 3 is not limited to the predictions of SoMs only for CYP-mediated metabolism but also for other types of phase I and phase II metabolism. Every SoM obtained by FAME 3 is characterized by probability score and FAME score (quality of prediction).

The software Glory uses the results obtained from FAME 2 to apply 73 reaction rules and generate the molecular structures of possible metabolites formed by CYP isoforms. Priority score for predicted metabolites is based on predicted SoM probabilities and the literature-based distinction between common and uncommon reaction types. In Glory, predicted

metabolites for a particular molecule are ranked by priority score which is calculated according to the SoM probability of atoms involved in the transformation and commonness of reaction.

The results of the calculations are given in **Table 8** and **Scheme 5**. Regarding compound **1**, both FAME 3 and Glory gave consistent results. The most probable metabolite is the one with a hydroxyl group in the C24 position. According to Glory, dealkylation at N9, hydroxylation at N9 as well as hydroxylation at C10 have the same probability to occur, however FAME 3 alone predicts the greater possibility of hydroxylation at site C10. For compounds **2**, **3** and **4** Glory indicates the amine fragment (**a3**) as a primary site of transformation; C12, C13 and N11 are centers most likely to undergo hydroxylation, as well as deamination of N11. Regarding other probable SoM and metabolites, compound **4** is more likely to undergo a transformation of the *n*-Bu group rather than at C21 (very low probability according to FAME 3). On the other hand, in the case of compound **2**, according to FAME 3, C21 is most likely to undergo hydroxylation, the same as in the case of compound **1**. According to FAME3, *i*-Pr –CH_3 is the prime site for the transformation of compound **3**. For compound **5,** transformations of the β-tetralinyl substituent, *i.e.* hydroxylation at C31, C32 and C34 are preferable compared to the ones suggested to the transformations within the amine fragment **a2**.

Table 8. The results of the calculation of the SoM by FAME 3 and Glory, h – stands for hydroxylation and da – stands for dealkylation

Compound	SoM	FAME 3		Glory
		Probability	FAME score	
1	**N9**	0.179	0.583	h: 2.93 da: 2.93
	C10	0.392	0.627	2.93
	C24	0.516	0.627	3.41
2	**N11**	0.448	0.453	h: 4.21 da: 4.21
	C12/C13	0.304	0.500	4.21
	C21	0.255	0.604	3.39
3	**N11**	0.336	0.453	h: 4.19 da: 4.19
	C12/C13	0.380	0.500	4.19
	C22	0.464	0.566	1.97
	C23/C24	0.828	0.650	-
	C31	0.430	0.620	2.25
4	**N11**	0.232	0.453	h: 4.18 da: 4.18
	C12/C13	0.220	0.500	4.18
	C32	0.555	0.587	1.93

5	**C13**	0.159	0.655	2.64
	C31	0.512	0.665	3.01
	C32	0.616	0.679	1.90
	C34	0.383	0.665	1.98

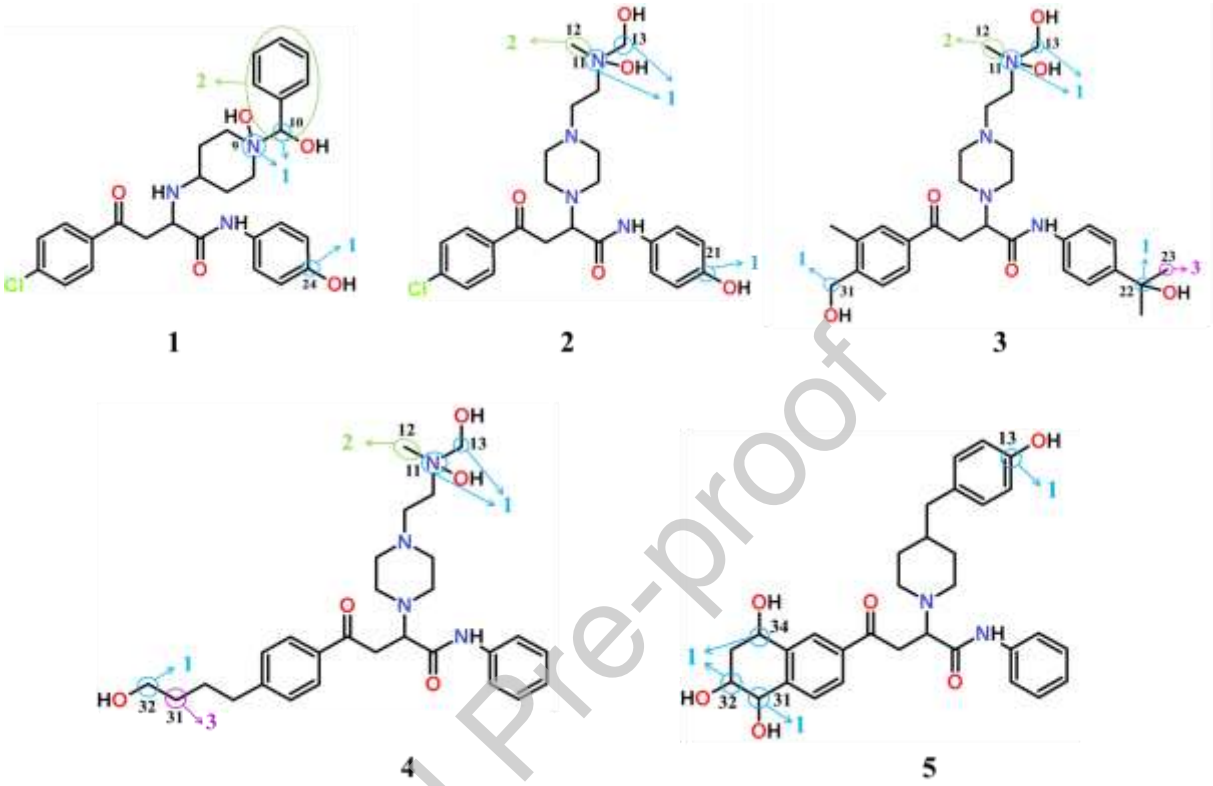

Scheme 5. Structures of putative metabolites of **1**-**5**. Blue circles represent sites of hydroxylation, green circles represent sites of amine group dealkylation according to Glory and violet circles are SoM's according to FAME3, but not recognized by Glory. The SoM estimated by FAME 3 nicely correspond to the structures proposed by the Glory program (atom numbering according to FAME 3).

3.5.3. SwissTarget prediction of probable macromolecular targets for compounds **1-5**

The probable macromolecular targets for compounds **1-5** were estimated using SwissTarget software, and the results are given in **Table 9**. The 100 biological targets were retrieved for each compound. All suggested targets for all compounds had a low probability score of 10-12%, so the software did not provide some comprehensive data about the possible targets. This is probably because of the relatively low structural similarity of our compounds compared to the ones used in the SwissTarget database. However, the relative percentage of the different target classes was different for **1**-**5**. For compounds **1** and **5**, the highest percentage of the proposed targets belong to the A class of G protein coupled receptors, while for compounds **2**, **3** and **4** the highest percentage of the proposed targets falls into the kinase family of enzymes.

Table 9. The estimated percentage of the biological target classes for the first hundred biological targets for compounds **1**-**5**, calculated by SwissTarget software.

Compound	Target class (%)						
	Kinase	**GPCR(A)**	**Enzyme**	**Protease**	**Electrochemical transporter**	**Voltage gated ion channel**	**Phospho-diesterase**
1	31	40	5	7	5	2	2
2	67	16	7	6	2	/	2
3	52	16	7	6	1	4	/
4	52	16	7	6	2	1	3
5	28	33	4	6	3	6	6

3.6. Possible structure-activity relationships for **1**-**5**

Although there are only five compounds under investigation, some structure-activity observations can be derived. The sequences of proapoptotic potency of **1**-**5** toward A549 and LoVo cell lines are similar: the most potent compound is **4**, while **1** is the least active. The situation for Skov-3 is different. In this case, compound **2** has the highest proapoptotic activity closely followed by compound **4**. The most distinctive difference is present for compound **5**, which is the least potent derivative toward the Skov-3 cell line but was fairly potent toward A549 and LoVo cell lines. From such analysis, it is evident that compounds that bear **a3** piperazine fragment, unsubstituted phenyl ring, and substituent at *p*-position (-Cl or *n*-Bu group) at aroyl ring, such as **2** and **4** were the most active toward all cell lines. The replacement of **a3** moiety with **a1,** such as seen in compound **1,** results in a significant decrease in anticancer potency (regardless of the type of cell death) toward all cell lines. Therefore, the nature of the cyclic amine moiety at position C2 of the compounds is probably the primary determinant of anticancer activity toward tested cell lines. The compounds' ability to raise MFI values, *i.e.*, the levels of $^{\bullet}O_2^-$ per cell, is also highest for compounds **2** and **4**, in A549 and LoVo cell lines.

Based on the results of all conducted biological assays, the most promising derivatives for further structural optimization seem to be compounds **4** and **5**. Compound **4** had the highest anticancer potency toward all cell phenotypes, and the apparent apoptotic cell death was the consequence of intrinsic apoptotic pathway activation. Undoubtedly, compound **4** was the only one that sharply increased $^{\bullet}O_2^-$ generation in all cell lines. Therefore, the overflow of the mitochondrial $^{\bullet}O_2^-$ may be proposed as one of the mechanisms for the induction of apoptotic response by **4** in all cancer cell phenotypes. The major drawback of this compound is significant toxicity toward *Artemia salina,* compound **4** being two times more toxic than the positive control potassium-dichromate. On the other hand, compound **5** displayed prooxidant ability at the least extent compared to all other compounds, revealed favorable anticancer

activity on all treated cell lines, and was the only one that triggered activation of intrinsic and extrinsic apoptotic pathways independently of each other. In the A549 cell line, **5** initiated exclusively apoptotic cell death at all tested concentrations in LoVo and Skov-3 cell lines at higher concentrations. Moreover, **5** was the most efficient in supressing cellular migration and was less toxic toward brine shrimp than **4**, **1**, and potassium-dichromate. All these facts highlight compound **5** as a promising lead for further optimization. The other three compounds were moderately potent toward all three cell lines and moderately toxic toward brine shrimp. The least promising was compound **1**, which was in most of the cases the least potent as an anticancer agent but the most toxic toward *Artemia salina*.

Thus, some conclusions about structure-activity relationships might be drawn. The most substantial influence on the anticancer activity of the compounds belongs to the cyclic amino fragment at position C2. The compounds bearing **a3** moiety were the most potent but also the most toxic. The substitution of **a3** with **a2** retained moderately potent anticancer activity with a significant reduction in toxicity, while the compound with **a1** moiety at position C2 was the least potent and the most toxic. Of the compounds that had **a3** moiety, the one that had 4-*i*-Pr substituent on the phenylamide ring, showed both reduction in anticancer activity and also in toxicity. Therefore, future structural modifications of these congeneric series of the compounds should include **a2** or **a3** fragment on the C2 position, and the optimal ratio of the anticancer potency/toxicity should be modulated by the substituents on the aroyl and phenylamide rings.

4. Conclusions

In summary, we designed and synthesized five Michael's adducts of secondary cyclic amines on aroylacrylic acid phenylamides. Three different amines were used: 1-amino-*N*-benzylpiperidine (**a1**), 4-benzylpiperidine (**a2**), and *N*,*N*-dimethyl-*N*-[2-(1-piperazinyl)-ethyl]amine (**a3**). All synthesized derivatives exerted anticancer activity in the micromolar range, toward all tested cancer phenotypes, mainly causing cell death *via* an intrinsic apoptotic pathway and accumulation of the cells at the S phase of mitotic division. Activation of the intrinsic apoptotic pathway might be a direct consequence of enhanced mitochondrial $^{\bullet}O_2^-$ generation, but the additional investigation should be carried out to confirm this hypothesis. The replacement of **a3** moiety with **a1**, such as seen in compound **1**, results in a significant decrease in anticancer activity toward all cell lines. Therefore, the nature of the cyclic amine moiety at position C2 of the compounds is probably the primary determinant of anticancer activity toward malignant cells. The antibacterial activity was also investigated.

Compounds **1** and **4** were one order of magnitude more potent than chloramphenicol in almost all investigated bacterial strains except for *S. aureus* and *B. subtilis*. The calculated ADME-Tox properties by several on-line available software tools show that most of the compounds have good pharmacokinetics and drug-like properties. Further structural modifications of the compounds which bear **a2** or **a3** amine moiety are underway to design more potent compounds for pro-apoptotic activity.

Funding: This work was supported by the Serbian Ministry of Defense. M.V. T., I.C., M.N., T. V., I.N. and S.B. acknowledge financial support from the Ministry of Education, Science and Technological development of Serbia, Contract numbers: 451-03-9/2021-14/200325, 451-03-9/2021-14/200168, 451-03-68/2021-14/200026, 451-03-68/2021-14/200043.

Conflict of interest: The authors declare that they have no conflict of interest.

Ethical standards: The manuscript does not contain clinical studies or patient data.

Credit author statement

T. Vujatović: Investigation, Writing – Original Draft, Visualisation. **M. Vitorović-Todorović**: Conceptualization, Methodology, Writing – Original Draft, Supervision. **I. Cvijetić**: Investigation, Writing – Review & Editing. **M. Nikolić**: Writing – Review & Editing, **T. Vasović**: Investigation**. I. Novaković:** Investigation, Writing – Review & Editing. **S. Bjelogrlić**: Conceptualisation, Investigation, Writing – Original Draft, Writing – Review & Editing, Supervision

References

[1] P. W. Snijman *et al.*, "Antioxidant Activity of the Dihydrochalcones Aspalathin and Nothofagin and Their Corresponding Flavones in Relation to Other Rooibos (Aspalathus linearis) Flavonoids, Epigallocatechin Gallate, and Trolox," *J. Agric. Food Chem.*, vol. 57, no. 15, pp. 6678–6684, Aug. 2009, doi: 10.1021/jf901417k.

[2] M. Bazzaro *et al.*, "α,β-Unsaturated carbonyl system of chalcone-based derivatives is responsible for broad inhibition of proteasomal activity and preferential killing of human papilloma virus (HPV) positive cervical cancer cells," *J. Med. Chem.*, vol. 54, no. 2, pp. 449–456, 2011, doi: 10.1021/jm100589p.

[3] C. R. Yellaturu, M. Bhanoori, I. Neeli, and G. N. Rao, " N-Ethylmaleimide Inhibits Platelet-derived Growth Factor BB-stimulated Akt Phosphorylation via Activation of Protein Phosphatase 2A ," *J. Biol. Chem.* , vol. 277, no. 42, pp. 40148–40155, Oct.

2002, doi: 10.1074/jbc.M206376200.

[4] L. H. Jensen *et al.*, "Maleimide is a potent inhibitor of topoisomerase II in vitro and in vivo: a new mode of catalytic inhibition," *Mol. Pharmacol.*, vol. 61, no. 5, pp. 1235–1243, 2002, doi: 10.1124/mol.61.5.1235.

[5] A. Massarotti, A. Coluccia, R. Silvestri, G. Sorba, and A. Brancale, "The Tubulin Colchicine Domain: a Molecular Modeling Perspective," *ChemMedChem*, vol. 7, no. 1, pp. 33–42, Jan. 2012, doi: 10.1002/cmdc.201100361.

[6] B. J. Leslie, C. R. Holaday, T. Nguyen, and P. J. Hergenrother, "Phenylcinnamides as Novel Antimitotic Agents," *J. Med. Chem.*, vol. 53, no. 10, pp. 3964–3972, May 2010, doi: 10.1021/jm901805m.

[7] B. J. Drakulić, T. P. Stanojković, Ž. S. Žižak, and M. M. Daković, "Antiproliferative activity of aroylacrylic acids. Structure-activity study based on molecular interaction fields," *Eur. J. Med. Chem.*, vol. 46, no. 8, pp. 3265–3273, 2011, doi: https://doi.org/10.1016/j.ejmech.2011.04.043.

[8] M. D. Vitorović-Todorović *et al.*, "(E)-4-Aryl-4-oxo-2-butenoic acid amides, chalcone-aroylacrylic acid chimeras: Design, antiproliferative activity and inhibition of tubulin polymerization," *Eur. J. Med. Chem.*, vol. 62, 2013, doi: 10.1016/j.ejmech.2013.01.006.

[9] P. H. Wiernik, "Alvocidib (flavopiridol) for the treatment of chronic lymphocytic leukemia," *Expert Opin. Investig. Drugs*, vol. 25, no. 6, pp. 729–734, Jun. 2016, doi: 10.1517/13543784.2016.1169273.

[10] C. Xi, L. Wang, J. Yu, H. Ye, L. Cao, and Z. Gong, "Inhibition of cyclin-dependent kinases by AT7519 is effective to overcome chemoresistance in colon and cervical cancer," *Biochem. Biophys. Res. Commun.*, vol. 513, no. 3, pp. 589–593, 2019, doi: https://doi.org/10.1016/j.bbrc.2019.04.014.

[11] K. McKeage, "Alectinib: A Review of Its Use in Advanced ALK-Rearranged Non-Small Cell Lung Cancer," *Drugs*, vol. 75, no. 1, pp. 75–82, 2015, doi: 10.1007/s40265-014-0329-y.

[12] M. Guha, "Imbruvica—next big drug in B-cell cancer—approved by FDA," *Nat. Biotechnol.*, vol. 32, no. 2, pp. 113–114, 2014, doi: 10.1038/nbt0214-113.

[13] P. Goel, O. Alam, M. J. Naim, F. Nawaz, M. Iqbal, and M. I. Alam, "Recent advancement of piperidine moiety in treatment of cancer- A review," *Eur. J. Med. Chem.*, vol. 157, pp. 480–502, 2018, doi: https://doi.org/10.1016/j.ejmech.2018.08.017.

[14] 2000. 1. National Committee for Clinical Laboratory Standards, Approval Standard

Document M7-A5, Villanova, Pa, USA, “No Title.”

[15] A. Sartoratto, A. L. M. Machado, C. Delarmelina, G. M. Figueira, M. C. T. Duarte, and V. L. G. Rehder, “Composition and antimicrobial activity of essential oils from aromatic plants used in Brazil,” *Brazilian J. Microbiol.*, vol. 35, no. 4, pp. 275–280, 2004, doi: 10.1590/S1517-83822004000300001.

[16] M. S. BLOIS, “Antioxidant Determinations by the Use of a Stable Free Radical,” *Nature*, vol. 181, no. 4617, pp. 1199–1200, 1958, doi: 10.1038/1811199a0.

[17] D. E. V Pires, T. L. Blundell, and D. B. Ascher, “pkCSM: Predicting Small-Molecule Pharmacokinetic and Toxicity Properties Using Graph-Based Signatures,” 2015, doi: 10.1021/acs.jmedchem.5b00104.

[18] S. Martin *et al.*, “FAME 3: Predicting the Sites of Metabolism in Synthetic Compounds and Natural Products for Phase 1 and Phase 2 Metabolic Enzymes,” *J. Chem. Inf. Model.*, vol. 59, no. iii, pp. 3400–3412, 2019, doi: 10.1021/acs.jcim.9b00376.

[19] J. Kirchmair, “GLORY : Generator of the Structures of Likely Cytochrome P450 Metabolites Based on Predicted Sites of Metabolism,” vol. 7, no. June, pp. 1–15, 2019, doi: 10.3389/fchem.2019.00402.

[20] A. Daina, O. Michielin, and V. Zoete, “SwissTargetPrediction: updated data and new features for efficient prediction of protein targets of small molecules,” *Nucleic Acids Res.*, vol. 47, no. W1, pp. W357–W364, Jul. 2019, doi: 10.1093/nar/gkz382.

[21] D. Gfeller, O. Michielin, and V. Zoete, “Shaping the interaction landscape of bioactive molecules,” *Bioinformatics*, vol. 29, no. 23, pp. 3073–3079, Dec. 2013, doi: 10.1093/bioinformatics/btt540.

[22] H. Murad *et al.*, “Induction of G1-phase cell cycle arrest and apoptosis pathway in MDA-MB-231 human breast cancer cells by sulfated polysaccharide extracted from Laurencia papillosa,” *Cancer Cell Int.*, vol. 16, no. 1, p. 39, 2016, doi: 10.1186/s12935-016-0315-4.

[23] R. Visconti, R. Della Monica, and D. Grieco, “Cell cycle checkpoint in cancer: a therapeutically targetable double-edged sword,” *J. Exp. Clin. Cancer Res.*, vol. 35, no. 1, p. 153, 2016, doi: 10.1186/s13046-016-0433-9.

[24] S. P. Jackson and J. Bartek, “The DNA-damage response in human biology and disease,” *Nature*, vol. 461, no. 7267, pp. 1071–1078, 2009, doi: 10.1038/nature08467.

[25] U. S. Srinivas, B. W. Q. Tan, B. A. Vellayappan, and A. D. Jeyasekharan, “ROS and the DNA damage response in cancer,” *Redox Biol.*, vol. 25, p. 101084, 2019, doi: https://doi.org/10.1016/j.redox.2018.101084.

[26] D. B. Zorov, M. Juhaszova, and S. J. Sollott, “Mitochondrial Reactive Oxygen Species (ROS) and ROS-Induced ROS Release,” *Physiol. Rev.*, vol. 94, no. 3, pp. 909–950, Jul. 2014, doi: 10.1152/physrev.00026.2013.

[27] D. Munro and J. R. Treberg, “A radical shift in perspective: mitochondria as regulators of reactive oxygen species,” *J. Exp. Biol.*, vol. 220, no. 7, pp. 1170 LP – 1180, Apr. 2017, doi: 10.1242/jeb.132142.

[28] K. Järvinen *et al.*, “Antioxidant defense mechanisms of human mesothelioma and lung adenocarcinoma cells,” *Am. J. Physiol. Cell. Mol. Physiol.*, vol. 278, no. 4, pp. L696–L702, Apr. 2000, doi: 10.1152/ajplung.2000.278.4.L696.

[29] H. Piotrowska, M. Kucinska, and M. Murias, “Expression of CYP1A1, CYP1B1 and MnSOD in a panel of human cancer cell lines,” *Mol. Cell. Biochem.*, vol. 383, no. 1–2, pp. 95–102, 2013, doi: 10.1007/s11010-013-1758-8.

[30] C. Lennicke, J. Rahn, R. Lichtenfels, L. A. Wessjohann, and B. Seliger, “Hydrogen peroxide – production, fate and role in redox signaling of tumor cells,” *Cell Commun. Signal.*, vol. 13, no. 1, p. 39, 2015, doi: 10.1186/s12964-015-0118-6.

[31] L. J. Marnett, “Oxyradicals and DNA damage,” *Carcinogenesis*, vol. 21, no. 3, pp. 361–370, Mar. 2000, doi: 10.1093/carcin/21.3.361.

[32] M. Michael and M. M. Doherty, “Tumoral Drug Metabolism: Overview and Its Implications for Cancer Therapy,” *J. Clin. Oncol.*, vol. 23, no. 1, pp. 205–229, Jan. 2005, doi: 10.1200/JCO.2005.02.120.

[33] E. A. Zaal and C. R. Berkers, “The Influence of Metabolism on Drug Response in Cancer ,” *Frontiers in Oncology* , vol. 8. p. 500, 2018, [Online]. Available: https://www.frontiersin.org/article/10.3389/fonc.2018.00500.

[34] M. Redza-Dutordoir and D. A. Averill-Bates, “Activation of apoptosis signalling pathways by reactive oxygen species,” *Biochim. Biophys. Acta - Mol. Cell Res.*, vol. 1863, no. 12, pp. 2977–2992, 2016, doi: https://doi.org/10.1016/j.bbamcr.2016.09.012.

[35] G. S. Salvesen and C. M. Walsh, “Functions of caspase 8: The identified and the mysterious,” *Semin. Immunol.*, vol. 26, no. 3, pp. 246–252, 2014, doi: https://doi.org/10.1016/j.smim.2014.03.005.

[36] A. Hallas-Potts, J. C. Dawson, and C. S. Herrington, “Ovarian cancer cell lines derived from non-serous carcinomas migrate and invade more aggressively than those derived from high-grade serous carcinomas,” *Sci. Rep.*, vol. 9, no. 1, pp. 1–10, 2019, doi: 10.1038/s41598-019-41941-4.

[37] F. Kroschinsky *et al.*, “New drugs, new toxicities: severe side effects of modern

targeted and immunotherapy of cancer and their management," *Crit. Care*, vol. 21, no. 1, p. 89, 2017, doi: 10.1186/s13054-017-1678-1.

[38] N. Damjanov, "Anticancer Drug Toxicity: Prevention, Management, and Clinical Pharmacokinetics," *Mod. Pathol.*, vol. 13, no. 9, p. 953, 2000, doi: 10.1038/modpathol.3880173.

[39] N. R. Filipović *et al.*, "Selenotriapine – An isostere of the most studied thiosemicarbazone with pronounced pro-apoptotic activity, low toxicity and ability to challenge phenotype reprogramming of 3-D mammary adenocarcinoma tumors," *Arab. J. Chem.*, vol. 13, no. 1, pp. 1466–1489, 2020, doi: https://doi.org/10.1016/j.arabjc.2017.11.017.

[40] B. L. Viega, A. M. Rocha, and E. Düsman, "Cosmetics with hormonal composition for bioindicators Artemia salina L. and Allium cepa L. toxic potential," *Environ. Sci. Pollut. Res.*, vol. 27, no. 6, pp. 6659–6666, 2020, doi: 10.1007/s11356-019-07392-0.

[41] S. Subhadra, V. R. Kanacharalapalli, V. K. Ravindran, S. K. Parre, S. Chintala, and R. Thatipally, "Comparative toxicity assessment of three Tephrosia species on Artemia salina and animal cell lines," vol. 2, no. 3, 2011, doi: 10.4103/2229-5119.86262.

[42] S. Muthukrishnan, T. Senthil Kumar, and M. V Rao, "Anticancer activity of biogenic nanosilver and its toxicity assessment on Artemia salina- evaluation of mortality, accumulation and elimination: An experimental report," *J. Environ. Chem. Eng.*, vol. 5, no. 2, pp. 1685–1695, 2017, doi: https://doi.org/10.1016/j.jece.2017.03.004.

[43] C. A. Lipinski, "Lead- and drug-like compounds: the rule-of-five revolution," *Drug Discov. Today Technol.*, vol. 1, no. 4, pp. 337–341, 2004, doi: https://doi.org/10.1016/j.ddtec.2004.11.007.